A transcription factor-responsive enhancer discovery platform for targeted immunotherapy

Yingbo Jia[1,2,9], Chu-Yen Chen[1,9], Bo Zhu[1,2,3,9], Zhigui Wu[1,4], Yi-Chia Wu[1,6,7], Renqi Wang[1,2], Abdulmajeed I. Salamah[1], Sushmita Halder[1], Yen-Nien Liu[1,5], Luca Scimeca[1,2], Hang Yin[1,2], Tejas Sabu[1], Enoch B. Antwi[1,2], Yang Wang[1,2,8], Ming-Ru Wu[1,2,*]

[1]Department of Cancer Immunology and Virology, Dana-Farber Cancer Institute, Boston, MA 02215, USA.

[2]Department of Immunology, Harvard Medical School, Boston, MA 02115, USA.

[3]Department of Liver Surgery, Center of Hepato-Pancreato-Biliary Surgery, Institute of Precision Medicine, The First Affiliated Hospital, Sun Yat-sen University, Guangzhou 510080, China.

[4]Department of Pharmacy, Affiliated Hospital, Southwest Medical University, Luzhou 646000, China.

[5]Graduate Institute of Cancer Biology and Drug Discovery, College of Medical Science and Technology, Taipei Medical University, New Taipei City 235, Taiwan.

[6]Department of Surgery, College of Medicine, Kaohsiung Medical University, Kaohsiung, Taiwan.

[7]Division of Plastic and Reconstructive Surgery/Breast Oncology and Surgery, Department of Surgery, Kaohsiung Medical University Hospital, Kaohsiung, Taiwan.

[8]West China School of Pharmacy, Sichuan University, Chengdu 610041, China.

[9]These authors contributed equally.

*Corresponding author. Email: ming-ru_wu@dfci.harvard.edu

Abstract

Synthetic enhancers with high specificity are crucial for therapeutic gene control. Although existing experimental screens and machine learning-based designs have advanced their discovery, these strategies remain context-restricted, typically requiring new cell-type- or state-specific libraries or datasets for each context, thus limiting their generalizability and scalability for broad biomedical applications. Because transcription factor (TF) activity naturally varies across cell types and cellular states, a high-coverage library of TF-responsive synthetic enhancers provides a universal starting point for identifying cell-type- or state-specific elements across diverse biological contexts. Harnessing this principle, we developed the TREND (transcription factor-responsive enhancer discovery) platform, a massively parallel reporter assay framework comprising 57,715 designs covering 1,068 TFs. To demonstrate its utility, we applied TREND to ovarian cancer and identified cancer-selective synthetic enhancers that discriminate cancer cells from normal epithelial cells. Building on these synthetic enhancers, we developed a protein-interaction-based AND-gate circuit that enables tighter control and enhanced transcriptional strength. In murine ovarian cancer models, these synthetic enhancers and AND-gate circuits achieved tumor-restricted activity and potent antitumor efficacy when driving combinatorial immune payloads. Extending TREND to immune cell engineering, we identified synthetic enhancers with stronger inducibility in the activated state and lower basal activity than conventional NFAT-motif-based enhancers in T cells. Together, these findings position TREND as a more generalizable framework for identifying synthetic enhancers with high contextual specificity, offering a versatile tool for precise gene regulation and context-aware therapeutic design.

Introduction

Enhancers orchestrate cell type- and state-specific transcriptional programs by integrating the activity of multiple transcription factors (TFs)[1,2]. This intrinsic logic makes them powerful elements for engineering precise gene control. The importance of such precision is particularly evident in oncology and cell-based immunotherapies. In cancer gene therapy, restricting transgene expression to cancer cells enhances tumor specificity and reduces collateral effects on normal tissues. In immune-based therapies, confining expression to activated rather than resting immune cells ensures that effector functions are triggered only upon antigen engagement, preventing premature or systemic immune activation[3,4]. Motivated by this need, synthetic biology has sought to harness enhancer activity to achieve context-specific gene expression that maximizes efficacy while minimizing off-target effects[5].

Existing experimental approaches, such as massively parallel reporter assays (MPRAs) and self-transcribing active regulatory region sequencing (STARR-seq), have enabled large-scale functional screening of regulatory elements and identified enhancers with improved specificity in selected contexts[6-11]. However, these libraries are typically constructed from regulatory regions of a given cell type or sequence set, which restricts their applicability and limits generalizability across diverse cellular states or disease settings. In parallel, recent advances in machine learning have shown that computational models can design cell-type-specific synthetic enhancers with high accuracy, achieving successful validation in mammalian systems[12-14]. Nevertheless, these strategies rely heavily on high-quality training datasets derived from accessible or active regulatory regions in the relevant cell type, which are often limited to particular developmental or steady-state contexts, and new applications typically require generating fresh datasets or retraining the model. As a result, it remains unclear whether such models can generalize to diverse disease settings, particularly cancer, where transcriptional networks are frequently rewired. Together, these limitations highlight the need for a broadly applicable framework capable of directly identifying synthetic enhancers with cell type and state specificity.

Since TF activity varies substantially between cell types and states, these differences represent a natural code that can be used to distinguish cellular identities[15,16]. If a synthetic enhancer is designed in response to a given TF, its activity will highly depend on whether that TF is active in a specific context[17]. Therefore, we reasoned that a library that encompasses a wide range of TF-responsive synthetic enhancers would increase the likelihood that a subset of elements

matches the active TFs in a given cell type. Screening such a high-coverage library could offer a direct way to identify cell-type-specific enhancers without requiring prior knowledge of cis-regulatory element (CRE) datasets or pre-trained computational models.

To this end, we developed TREND, a transcription factor-responsive enhancer discovery platform built upon a lentiviral MPRA framework. The system comprises 57,715 synthetic enhancer designs responsive to 1,068 TFs with known binding motifs, providing broad coverage across the TF landscape. By assaying activity directly in context-relevant cells, TREND harnesses native transcriptional logic and enables unbiased identification of synthetic enhancers with high specificity across diverse cell types and cellular states. In this study, we present TREND as a broadly applicable framework for the discovery of highly specific synthetic enhancers, exemplified by cancer-selective and T cell activation-responsive elements. We further demonstrate that these enhancers can be integrated into diverse synthetic biology applications, including logic-gated gene circuit design and in vivo cancer immunotherapy.

Results

TREND platform identifies candidate cancer-selective synthetic enhancers

To enable high-throughput screening of synthetic enhancers, we developed the TREND platform, based on a lentiviral MPRA framework[6,18]. To maximize the responsiveness of synthetic enhancers to individual TF, each construct was designed to contain tandem repeats of a single TF binding site (TFBS). Therefore, to generate potential TFBS for synthetic enhancer design, we first collected position probability matrices (PPMs) and position weight matrices (PWMs) for 1,068 human TFs from 14 public databases[19], including ENCODE, JASPAR, and CIS-BP (Fig. 1a). This library covered 1,068 of the 1,107 TFs with known binding sites (96.5% coverage)[16], including a large proportion of both cell-identity factors and pan-cancer master regulators (Fig. 1b)[20,21]. By encompassing nearly all TF with known binding motifs, the library provides an extensive set of TF-responsive synthetic enhancers, which can be applied across a wide range of cellular and disease settings.

As TF binding motifs exhibit substantial diversity and context-dependent affinities[22,23], we hypothesized that motif variants could yield distinct binding strengths, activation thresholds, and enhancer activities. To capture this range, we extracted the ten most probable sequences from each PPM or PWM, with the highest-probability sequence representing the consensus and the next nine

treated as variants. Each synthetic enhancer design consisted of tandem repeats of a single TFBS placed upstream of an adenoviral minimal promoter driving EGFP expression and linked to a unique DNA barcode[17,24]. By combining thousands of these individual constructs, we generated a pooled library comprising 57,715 synthetic enhancer-reporter elements for high-throughput screening.

To identify cancer-specific enhancers, the library was packaged into lentiviruses and introduced into human immortalized ovarian surface epithelium cells (IOSE), human ovarian cancer (OVCAR-8; OV8) cells, and murine ovarian cancer (ID8) cells. IOSE cells were used as a surrogate for normal ovarian surface epithelium because they retain key epithelial features and transcriptional similarity to primary ovarian surface epithelial cells while allowing efficient lentiviral transduction and high-coverage screening[25]. To quantify synthetic enhancer activity, we measured barcode abundance in both RNA and DNA by targeted next-generation sequencing (NGS). Each enhancer was associated with multiple unique barcodes, providing independent readouts of its activity. This design helps account for variability introduced by lentiviral integration site effects, intrinsic transcriptional noise, and potential enhancer-barcode mismatches, thereby reducing the influence of outliers. For each enhancer, we first calculated the RNA/DNA ratio for every individual barcode, and then used the median value across all associated barcodes as the final measure of enhancer activity. This approach ensured a robust and accurate quantification of enhancer-driven expression in both normal and cancer contexts. Finally, the mean values of biological replicates were used to represent the overall activity for each construct.

Based on these barcode-derived activity scores, each synthetic enhancer can be classified as preferentially active in normal cells or cancer cells, broadly active in both, or inactive in both contexts. Sequencing data were processed through a standardized computational pipeline that included read demultiplexing to separate samples, unique molecular identifier (UMI) collapsing to correct for PCR amplification bias, and alignment to the reference library to assign barcodes to their corresponding enhancer constructs. Transcript-per-million (TPM) normalization was then applied to correct for differences in sequencing depth across samples. Finally, stringent quality filters were used to remove low-confidence elements with insufficient barcode representation, ensuring accurate, robust, and reproducible measurements across the entire library (Fig. 1c). As a result of the broad and diverse library design, synthetic enhancer activity in IOSE and OV8 cells spanned a wide dynamic range. While most enhancers produced comparable output in both

contexts, a subset displayed high OV8/IOSE activity ratios, marking them as candidate cancer-specific synthetic enhancers (highlighted in red, Fig. 1d). Biological replicates showed highly concordant activity profiles, with strong inter-experimental correlations (Extended Data Fig. 1), supporting the robustness and reproducibility of the TREND platform.

To assess whether TF mRNA abundance could predict synthetic enhancer performance, we compared TF-guided enhancer activity with RNA-seq-based differential expression between OV8 and IOSE cells. No meaningful correlation was observed (Extended Data Fig. 2a), and the most cancer-selective enhancers identified by TREND did not correspond to TFs with the highest differential expression (Extended Data Fig. 2b). Conversely, enhancers associated with highly differentially expressed TFs did not exhibit high specificity (Extended Data Fig. 2c). These results indicate that relying on RNA-seq-based TF expression alone is insufficient for identifying functional, cell-type-specific enhancers, and highlight the value of direct screening approaches such as TREND for uncovering effective regulatory elements. Among the top cancer-specific enhancers, there was no clear relationship between enhancer performance and motif's rank within the PPM or PWM. Highly specific enhancers could arise from either the consensus sequence (highest-ranked motif) or from lower-ranked variants within the same matrix (Extended Data Fig. 2d). This finding suggests that motif rank alone cannot reliably predict which variants will yield the strongest specificity. Therefore, incorporating multiple motif variants per PPM or PWM is important, and our strategy of generating ten enhancer designs per matrix appears to provide greater diversity to capture a broader range of context-specific enhancers. Beyond identifying activators, TREND revealed multiple classes of synthetic enhancers, including those selectively active in human cancer cells (high OV8/IOSE), mouse cancer cells (high ID8/IOSE), and shared cancer-selective elements active in both human and mouse cancer cells (high OV8/IOSE and ID8/IOSE), as well as enhancers preferentially active in immortalized human epithelial cells (high IOSE/OV8, high IOSE/ID8, or both). These results highlight the versatility of TREND in identifying diverse, context-dependent enhancer activities across species and cellular states (Extended Data Fig. 2e). Collectively, these findings demonstrate that TREND enables direct functional assessment of synthetic enhancers, uncovering context-specific elements that are not predictable from TF expression or motif information alone.

Experimental validation of cancer-specific enhancer candidates identified by TREND

To confirm that the cancer-specific synthetic enhancer candidates identified by TREND are functionally active, we individually cloned the top hits and tested their activity in OV8 and IOSE cells. Quantitative reporter assays were performed by placing each enhancer upstream of an adenoviral minimal promoter driving EGFP, followed by lentiviral delivery into OV8 and IOSE cells. Several motif variants from the MYC and E2F families consistently showed strong activity in OV8 cells while remaining largely inactive in IOSE (Fig. 2a). Given their pronounced activity and cancer specificity, MYC_v4 and E2F_v2 were selected as representative synthetic enhancers for further analysis. When introduced into OV8 and IOSE cells, both enhancers produced strong and uniform fluorescence in OV8, whereas IOSE cells displayed only background-level signal (Fig. 2b). Together, these results suggest that TREND can nominate synthetic enhancers with robust and cancer-selective activity.

We next asked whether TREND-identified synthetic enhancers are functionally responsive to their intended TFs. To test this, we focused on two validated candidates, MYC_v4 and E2F_v2. Each enhancer was co-transduced with an inducible TF overexpression cassette, allowing TF abundance to be tuned by varying the inducer dose. Reporter assays in IOSE cells showed a clear dose-response: increasing MYC or E2F4 levels enhanced activity from the matched enhancer, whereas activity from the unmatched enhancer remained largely unchanged (Fig. 2c, d, Extended Data Fig. 3). While this experiment focused on two representative enhancers rather than the entire library, the dose-dependent increase in activity with cognate TF abundance aligns with the TFBS-guided design and is consistent with the expectation that TREND-nominated elements can reflect the activity of their corresponding TFs.

In our previous study, we demonstrated that synthetic enhancers can achieve higher specificity than native cancer-specific promoters[4]. To further evaluate whether TREND-derived synthetic enhancers provide improved functional performance over those earlier manually designed constructs, we compared the top-performing TREND candidates with our prior design. Reporter assay showed that TREND-derived synthetic enhancers drove stronger activity in cancer cells while maintaining markedly improved specificity (Fig. 2e,f). These findings demonstrate that TREND can identify synthetic enhancers with enhanced performance relative to prior designs, underscoring the value of a TF-guided high-throughput discovery strategy for generating functional, cancer-specific regulatory elements.

Protein interaction-based AND gate circuits

Although individual TREND-derived enhancers exhibited high cancer selectivity, residual activity in certain normal cells could still compromise therapeutic safety[26]. To mitigate this limitation, we engineered protein-interaction-based AND-gate circuits that integrate multiple TF inputs. While a single transcriptional marker may still show low-level activity in some normal cells, the probability that two distinct markers are active at the same time in a healthy cell is much lower. Consequently, AND-gate circuits could confine gene expression to cancer-specific contexts, minimizing off-target activity and enhancing safety.

To implement this logic, each TREND-derived enhancer was used to drive expression of one half of a split transcription factor: GAL4 DNA-binding domain (GAL4BD) fused to a leucine-zipper domain and VP16 activation domain (VP16AD) fused to its complementary partner. Only when both enhancers are active are the two components produced simultaneously, allowing them to associate and form a functional GAL4BD-VP16AD transcriptional activator (GAD, for GAL4BD-VP16AD complex). To identify the most effective leucine-zipper pairs for reconstitution, we assembled a library of 55 previously characterized heterodimeric coiled-coil domains, including the canonical SYNZIP set and additional validated interaction pairs from published studies[27,28] (Fig. 3a). All possible 55 × 55 combinations were tested in a pooled format, with each candidate fused to either the GAL4BD (GAL4BD-zipper) or the VP16AD (zipper-VP16AD). When two compatible zippers interact, the GAL4BD-zipper and zipper-VP16AD components associate to reconstitute a functional GAD, which activates a GAL4 promoter driving further expression of the same GAL4BD-zipper and zipper-VP16AD pair. This positive-feedback loop amplifies transcripts of interacting pairs, allowing their relative abundance to serve as a quantitative readout of interaction strength. Because HEK293T cells do not express GAD endogenously, we incorporated a Tet-ON inducible system to transiently provide baseline GAD activity across all cells[29]. This initial induction triggers low-level transcription of each candidate pair; if the paired zippers interact, they sustain and amplify their own expression through the feedback loop, whereas non-interacting pairs quickly decay after the initial induction (Fig. 3a).

To ensure that each cell expressed only one candidate pair, viral delivery was performed at low multiplicity of infection. RNA sequencing of zipper transcripts revealed a range of interaction strengths across all tested pairs (Fig. 3b). To capture this diversity, we selected several representative pairs spanning weak to strong interactions, as highlighted with circles in Fig. 3b,

for subsequent construction of AND gate circuits. Flow cytometry analysis showed that the SYNZIP5-SYNZIP12 combination produced the strongest reporter activation among the pairs examined (Fig. 3c). To confirm that our split-transcription factor design functions as a true AND gate, we first tested whether partial circuit configurations could activate the reporter. Each cell received three expression cassettes: two input modules encoding GAL4BD-SYNZIP2 and SYNZIP1-VP16AD under separate enhancers, and a third module in which the reconstituted GAD drives the mKate reporter. We evaluated three input combinations: [1,0] (only module 1 present), [0,1] (only module 2 present), and [1,1] (both modules present). Reporter expression was detected exclusively in the [1,1] condition, while [1,0] and [0,1] configurations showed no detectable signal (Extended Data Fig. 4a). These prototyping experiments were performed by transiently transfecting HEK293T cells to allow rapid and efficient circuit testing. The results confirm that the split-transcription factor architecture enforces stringent AND-gate logic and prevents leakage from individual input cassettes.

We next tested whether the same design remains functional when delivered by lentivirus for stable genomic integration, as intended for application in tumor models. The circuit components were introduced into both human OV8 and murine BPPNM ovarian cancer cells using lentiviral transduction. Reporter assays revealed robust activation in both lines (Extended Data Fig. 4b), demonstrating that the AND-gate circuit performs reliably in integrated formats across species. Furthermore, the output strength can be tuned by selecting different SYNZIP interaction pairs, highlighting the adjustable nature of the system. After selecting representative SYNZIP pairs, we next sought to determine how best to incorporate them into split TFs. Because the optimal positioning of SYNZIP domains within the split TF was unclear, we systematically evaluated three fusion configurations. Reporter assays revealed that transcriptional activation occurred only when the SYNZIP was fused to the C terminus of GAL4BD and the N terminus of VP16AD (Extended Data Fig. 4c,d). Alternative orientations failed to restore activity, emphasizing the importance of domain arrangement for complex reconstitution. Incorporating a nuclear localization signal (NLS) into VP16AD further enhanced reporter expression, indicating that efficient nuclear targeting improves transcriptional activation (Extended Data Fig. 4e).

To evaluate whether TREND-derived synthetic enhancers can serve as inputs for the AND-gate design, we selected six validated human ovarian cancer-specific enhancers (MYC_v4, E2F7_v3, MYC_v2, E2F_v2, FOS, and BACH1) and paired them systematically in all possible

two-input combinations (6 × 6 matrix). The schematic of the modular AND-gate circuit is shown in Fig. 3d: one synthetic enhancer drives the expression of GAL4BD fused to SYNZIP5 (module 1), and the other drives VP16AD fused to its complementary partner, SYNZIP12 (module 2). Transcriptional activation occurs only when both enhancers are active, allowing the two fusion proteins to assemble into a functional GAD that induces the expression of the downstream mKate reporter. Screening across the enhancer pair matrix identified several combinations that exhibited strong and cancer-restricted activity in OV8 cells while remaining largely inactive in IOSE cells (Fig. 3e,f; Extended Data Fig. 5a). These results demonstrate that specific TREND-derived enhancer pairs can cooperate through the AND-gate circuit to achieve highly cancer-selective transcriptional activation. Compared with our earlier AND-gate design reported previously[4], the current system achieved substantially higher specificity (Extended Data Fig. 5b). When compared with single-enhancer configurations, the AND-gate also amplified transcriptional output, producing stronger reporter expression and sharper cancer-to-normal discrimination (Extended Data Fig. 5c,d).

Because single synthetic enhancers can exhibit low-level background activity in certain normal cells, we further tested whether the AND-gate configuration could enhance targeting precision. From prior study, MYC- and E2F-based synthetic enhancers show minimal basal activity across various primary human cells (dermal fibroblasts, ovarian fibroblasts, and ovarian microvascular endothelial cells), non-tumorigenic breast cell lines (MCF-10A and MCF-12A), and induced pluripotent stem cells[4]. However, MYC-based enhancers displayed modest activity in a non-tumorigenic colonic epithelial cell line (CCD-841CoN), and E2F-based enhancers also exhibited modest basal activity in primary human T cells. To verify whether the AND-gate circuits can mitigate this effect, we compared the activity of single enhancers and AND-gate circuits in CCD-841CoN cells and primary T cells. While single-enhancer constructs showed notable activity, the AND-gate circuits exhibited minimal or no detectable activation (Extended Data Fig. 5e,f). Together, these findings establish that the AND-gate architecture driven by TREND-derived synthetic enhancers markedly enhances both the specificity and potency of context-dependent gene expression, providing a robust framework for precise transcriptional control.

Tumor-specific AND-gate gene circuits for combinatorial immunotherapy

Building on the cancer-specific AND-gate gene circuits, we next explored their potential as therapeutic platforms for cancer immunotherapy. To translate this design into a therapeutic context, we evaluated the constructs in vivo for their ability to drive potent and tumor-restricted immune responses.

To extend our system to murine models, we next applied the pipeline to the ID8 ovarian cancer cell line using IOSE cells as a reference to identify candidate mouse-specific synthetic enhancers (Extended Data Fig. 6a,b). The ID8 line is a well-established and widely used murine model of ovarian cancer, providing an accessible starting point for testing cross-species applicability and extending our system to in vivo studies. As the genetically defined BPPNM model later became available[30], we prioritized it for downstream studies because it better reflects the genomic alterations commonly observed in human ovarian cancer. To ensure broad coverage across model systems, we combined both human- and mouse-validated synthetic enhancers and evaluated their activity in BPPNM cells to identify cancer-selective candidates. We also tested these enhancers in two additional murine ovarian cancer models, KPCA and PPNM, which together with BPPNM represent a panel of genetically engineered models that capture the most frequent driver mutations found in patient ovarian tumors. From these analyses, several enhancer variants derived from the PPMs of ZBTB33 and MYC families showed the strongest and most consistent cancer-specific activity in BPPNM cells (Extended Data Fig. 6c-e). Because TF binding motifs can overlap or share sequence similarities, using highly related motifs as AND-gate inputs may cause signal crosstalk and reduce the precision of logical control. To minimize this effect, we selected two divergent enhancer variants, ZBTB33_v2 and MYC_v2, as inputs for constructing cancer-specific AND-gate circuits and prioritized them for proof-of-concept testing in the BPPNM ovarian cancer model.

We first assessed their safety and targeting precision in vivo, as both parameters are essential for clinical translation. BPPNM tumor-bearing mice and tumor-free wild-type C57BL/6 mice controls were intraperitoneally administered lentiviral vectors encoding luciferase under the control of the synthetic enhancers (Fig. 4a). Bioluminescence imaging revealed that luminescent signals were confined to tumor-bearing mice, with only background-level activity observed in healthy controls (Fig. 4b,c). To rule out poor viral delivery as a potential explanation for the absence of signal in normal tissues, we included a CMV promoter control, which drove widespread expression in the spleen, peritoneal wall, and tumor (Fig. 4d,e). In contrast, the AND-gate circuit

restricted luciferase activity to tumor sites. Together, these findings demonstrate that the AND-gate gene circuits achieve robust, tumor-selective activation with minimal off-target expression, highlighting their potential as a safe and effective platform for in vivo therapeutic applications.

We next applied the tumor-specific AND-gate circuit to drive combination immunotherapy. The same circuit architecture illustrated in Fig. 3c was used, except that the output module now expressed therapeutic effectors rather than fluorescent reporters (Extended Data Fig. 7). Effective antitumor immunity is often constrained by multiple, concurrent barriers within the tumor microenvironment, including limited tumor antigen engagement, poor T-cell co-stimulation, and suppressive signaling that dampens effector responses[31]. To potentially address these bottlenecks, we assembled a panel of immunomodulators designed to target complementary aspects of tumor immunity. The surface T-cell engager (STE), a tumor-displayed anti-CD3ε scFv that binds CD3 on T cells, was designed to promote direct T cell-tumor cell engagement, whereas CD80 provided a source of co-stimulatory signaling to enhance T-cell activation[32-34]. The cytokine IL-12 was included to support T_H1 polarization and effector differentiation, while Fms-related receptor tyrosine kinase 3 ligand (FLT3LG) was selected to expand dendritic cells (DCs) and facilitate antigen presentation[35,36]. CCL21 was incorporated to encourage immune cell recruitment to the tumor milieu[37]. In addition, the N-terminal fragment of Gasdermin D (GSDMD-N) was used to induce immunogenic tumor cell death, and an anti-PD-1 single-chain variable fragment (scFv) was designed to locally mitigate checkpoint inhibition and restore T-cell function[38,39].

Different combinations of these payloads, including SCIP (STE, CCL21, IL-12, anti-PD-1 scFv), S8FP (STE, CD80, FLT3LG, anti-PD-1 scFv), S8IP (STE, CD80, IL-12, anti-PD-1 scFv), SFIP (STE, FLT3LG, IL-12, anti-PD-1 scFv), S8GP (STE, CD80, GSDMD-N, anti-PD-1 scFv), and SFGP (STE, FLT3LG, GSDMD-N, anti-PD-1 scFv), were tested in the BPPNM ovarian cancer model to identify therapeutic modules capable of reducing tumor burden and reprogramming the tumor microenvironment. Mice receiving the S8IP combination exhibited prolonged survival compared with controls (Fig. 4f). Bioluminescence imaging confirmed reduced tumor burden, and quantification identified the S8IP module comprising STE, CD80, IL-12, and anti-PD-1 scFv as producing the strongest therapeutic effect (Fig. 4g,h). Increasing the dosage of this circuit treatment further enhanced tumor control and extended survival, demonstrating a dose-dependent therapeutic response (Fig. 4i,j). Together, these findings demonstrate that tumor-specific synthetic circuits capable of coordinating multiple immunomodulators can achieve robust therapeutic

benefit in vivo, supporting combination gene-circuit immunotherapy as a viable strategy to enhance antitumor efficacy.

Having demonstrated that the therapeutic circuits drive potent and tumor-restricted activity in vivo, we next examined how these treatments remodel the tumor microenvironment. Flow cytometry analysis of peritoneal immune cells revealed broad remodeling of immune composition following S8IP treatment (Fig. 4k). The proportions of total $CD4^+$ and $CD8^+$ T cells, central and effector memory T cell subsets, Granzyme B^+ cytotoxic $CD8^+$ T cells, and IFN-γ^+ T_H1 cells were markedly increased, indicating enhanced adaptive immune activation. In parallel, increased frequencies of total macrophages, M1-like macrophages, and DCs may indicate the myeloid compartment shifted toward an immunostimulatory phenotype[40-42]. Together, these findings demonstrate that S8IP treatment not only reduces tumor burden but also reshapes the tumor microenvironment toward a coordinated pro-inflammatory state that supports durable antitumor immunity.

To further characterize these responses, we analyzed additional immune subsets. Both $CD4^+$ and $CD8^+$ T cells exhibited increased proportion of PD-1^+ cells, a feature associated with recent activation as well as checkpoint regulation (Extended Data Fig. 8a). In the context of expanded effector populations and enhanced inflammatory responses, this increase most likely reflects active engagement rather than terminal exhaustion. Other populations, including natural killer (NK) cells, natural killer T (NKT) cells, cytotoxic NK cells, regulatory T (Treg) cells, $Ly6C^{high}$ monocytes, neutrophils, conventional type 1 dendritic cells (cDC1s) and cDC2s remained largely unchanged (Extended Data Fig. 8b,c). These results suggest that the therapeutic circuits act primarily through enhancing the T cell-mediated immunity and potentially myeloid effector activity, consistent with the design of the S8IP module, which was intended to augment T cell-mediated anti-tumor immune responses.

Taken together, these experiments demonstrate that TREND-derived synthetic enhancers integrated into AND-gate gene circuits can drive potent and tumor-restricted combination immunotherapy in vivo. By coordinating multiple immune effectors within a spatially confined genetic program, these circuits provide a robust and modular framework for safe and precise therapeutic gene control.

TREND platform identifies activation-responsive synthetic enhancers in T cells

To determine whether the TREND platform can be generalized beyond tumor targeting, we next applied it to immune cell engineering. In adoptive cell therapies such as chimeric antigen receptor (CAR) T-cell therapy, coupling transgene expression to T cell activation enables therapeutic payloads such as cytokines or immune modulators to be produced only upon antigen engagement, thereby potentially enhancing efficacy and minimizing systemic toxicity[3,43]. However, existing activation-responsive synthetic enhancers, particularly those based on multimerized NFAT binding motifs, often exhibit basal leakiness in resting T cells, leading to unwanted background expression that can trigger premature effector release or systemic immune activation[44,45]. Thus, developing synthetic enhancers with stronger induction and tighter off-state silencing remains an important goal.

To address this need, we used the TREND platform to identify synthetic enhancers that respond selectively and stringently to T cell activation. Because primary human T cells vary substantially across donors in proliferation, transduction efficiency, and activation sensitivity[46,47], we sought to discover robust enhancer elements that function reproducibly across multiple human donors rather than donor-specific ones. Primary human T cells from two independent donors were first activated and transduced with the pooled TREND lentiviral library. After returning to a resting state, cells were stimulated, and enhancer-driven reporter activity was quantified by NGS of barcode-linked transcripts (Fig. 5a). This workflow allowed direct comparison of enhancer activity between resting and activated states. From this screen, we identified a set of candidate activation-responsive enhancers, including NFKB1_v1, FOSL2, BCL, REL, RELA, FOSL1_v1, NFKB2, FOSL1_v2, NFKB1_v2, AP1_v3, AP1_v1, NFAT_v1, AP1_v2, and NFAT_v2, which showed strong induction upon T cell activation while remaining relatively silent in the resting state.

We next validated these candidates individually in primary human T cells from three different donors. Across donors, most enhancers displayed markedly higher activity in the activated state than in the resting state (Fig. 5b-c; Extended Data Fig. 9a-f). However, enhancers such as NFKB1_v1, BCL, REL, RELA, and NFKB1_v2 showed substantially higher basal EGFP expression than other candidates in resting T cells, indicating incomplete silencing under baseline conditions (Fig. 5d; Extended Data Fig. 9c, f). Among all tested elements, FOSL1_v1 consistently demonstrated the strongest activation specificity, producing robust reporter expression upon stimulation while maintaining near background activity in resting cells across all donors.

To ensure these results reflected enhancer-intrinsic regulation rather than differences in T cell activation, we measured expression of CD25, a canonical activation marker, and found comparable induction across all conditions (Extended Data Fig. 9g). This confirmed that variation in enhancer-driven reporter output arose from differences in regulatory performance rather than unequal activation efficiency. Finally, direct comparison with the conventional NFAT-motif-based enhancer showed that FOSL1_v1 achieved markedly lower basal expression in resting T cells while driving stronger reporter induction upon stimulation (Fig. 5e-j and Extended Data Fig. 10). T cells transduced with either construct exhibited similar CD25 expression, confirming equivalent activation states (Fig. 5h). Collectively, these data demonstrate that FOSL1_v1 provides tighter off-state control and higher inducibility than existing NFAT-motif-based designs, potentially offering a more precise transcriptional switch for regulating effector activity in engineered T cells.

Together, these findings demonstrated that TREND can be extended beyond tumor-targeting contexts to discover activation-responsive synthetic enhancers in primary human T cells, underscoring its versatility as a platform for discovering context-specific regulatory elements.

Discussion

Synthetic enhancers that enable precise, context-dependent gene expression are increasingly important for both fundamental biology and therapeutic engineering[48]. In this study, we developed TREND, a TF-guided screening framework designed to systematically identify synthetic enhancers with high cellular specificity and context-dependent activity, potentially providing a broadly applicable approach for precise gene control across diverse biological systems. Existing approaches for enhancer discovery often depend on cell-type-specific regulatory datasets, such as ATAC-seq, DNase-seq, or ChIP-seq-derived enhancer maps, or on computational models trained on those datasets[8,9,13,14,17]. While these methods can reliably recover enhancer activity in well-characterized contexts, they typically require new reference data or model retraining when applied to different cell types or disease states, which limits their flexibility.

Because TF activities vary across cell types and physiological states, assaying a broad library of TF-responsive sequences enables the native transcriptional environment to reveal which motifs are preferentially active in a given context. The TREND library comprises 57,715 variant synthetic enhancer designs representing 1,068 TFs, each constructed from tandem repeats of a single motif sequence derived from the PPM or PWM of that TF. When screened in a specific cell type, each

element serves as a functional reporter of endogenous transcriptional programs, linking cellular state to enhancer performance. By assaying motif-driven transcriptional activity directly in native cellular environments, TREND enables functional identification of synthetic enhancers with cell-type or state specificity, without relying on pre-annotated, context-specific regulatory libraries or computational models.

Applying TREND to human and murine ovarian cancer systems uncovered synthetic enhancers that robustly distinguished cancer cells from non-tumorigenic epithelial cells. Candidates derived from the MYC and E2F families displayed strong cancer-selective activity and responded quantitatively to the abundance of their cognate TFs. These results indicate that TREND-identified enhancers may serve as compact, modular reporters of disease-associated transcriptional programs. Compared with earlier manually designed synthetic enhancers[4], the TREND-derived elements exhibited both higher output and improved cancer selectivity.

Although a single TREND-derived enhancer often achieved strong specificity, low-level activity could occasionally be detected in non-malignant cells. To further tighten control, we implemented a protein-interaction-based AND-gate circuit that integrates signals from two enhancers. In this design, each enhancer drives one half of a split transcription factor (GAL4BD-SYNZIP and SYNZIP-VP16AD). Only when both enhancers are active do the two proteins interact through their coiled-coil SYNZIP domains to reconstitute a functional GAD and initiate transcription. This configuration enforces strict logical control, effectively suppressing background activation when one enhancer exhibits leakage while maintaining robust on-target expression when both enhancers are active, as demonstrated in Extended Data Fig. 5e,f.

We next established a proof-of-concept for in vivo application by using these synthetic enhancer-driven AND-gate circuits to coordinate therapeutic gene expression. In murine ovarian cancer models, cancer-specific enhancer pairs were combined to drive effector modules encoding complementary immune mediators. These circuits restricted activity to tumor sites, reduced overall tumor burden, and improved survival while promoting a pro-inflammatory tumor microenvironment. Among the tested configurations, the S8IP module (STE, CD80, IL-12, anti-PD-1 scFv) produced the strongest therapeutic response in a dose-dependent manner. These proof-of-concept results suggest that combining tumor-restricted synthetic enhancers through an AND-gate framework can achieve potent and spatially confined expression of immunomodulators for efficient cancer immunotherapy in mouse models. Future work focusing on identifying the

minimal synergistic effector combinations within S8IP while maintaining antitumor efficacy could reduce circuit output complexity. Moreover, integrating multiple circuit modules into one or two vectors may further simplify manufacturing and enable more precise control over component stoichiometry.

Extending TREND beyond tumor-targeted context, we applied it to primary human T cells to uncover synthetic enhancers that precisely couple transgene expression to T cell activation. The resulting constructs exhibited greater activation-dependent expression and lower basal activity than the conventional NFAT-motif-based promoter used in earlier cytokine-secreting CAR-T designs[43,44]. Among them, FOSL1_v1 reproducibly linked reporter expression to T cell stimulation across donors, providing a tighter transcriptional control module for engineered T cells that release payloads only upon activation. These results indicate that TREND can be applied across diverse biological contexts to identify synthetic enhancers with high contextual specificity.

While TREND is applicable across diverse contexts, several aspects could be further refined. First, the current study focuses on enhancers composed of single TF motifs in tandem, which simplifies design but does not explore cooperative or combinatorial motif architectures observed in natural regulatory elements[49,50]. Future studies integrating multiple motif types could provide additional tuning flexibility. In addition, incorporating machine-learning-guided optimization could help generate synthetic enhancers with improved performance beyond those currently represented in the library.

Overall, TREND offers a versatile experimental framework for discovering synthetic enhancers with strong contextual specificity. By directly assaying the transcriptional activity of diverse motif variants across cellular contexts, the approach provides a more scalable path to tailor gene-control elements for defined cellular or disease settings. This strategy may facilitate safer and more precise gene therapies, enhance the design of cell-based immunotherapies, and expand the toolkit for programmable synthetic biology.

Reference

1 Levo, M. & Segal, E. In pursuit of design principles of regulatory sequences. *Nat Rev Genet* **15**, 453-468, doi:10.1038/nrg3684 (2014).

2 Jolma, A. *et al.* DNA-binding specificities of human transcription factors. *Cell* **152**, 327-339, doi:10.1016/j.cell.2012.12.009 (2013).

3 Chen, A. X. Y. *et al.* Rewiring endogenous genes in CAR T cells for tumour-restricted payload delivery. *Nature* **644**, 241-251, doi:10.1038/s41586-025-09212-7 (2025).

4 Nissim, L. *et al.* Synthetic RNA-Based Immunomodulatory Gene Circuits for Cancer Immunotherapy. *Cell* **171**, 1138-1150 e1115, doi:10.1016/j.cell.2017.09.049 (2017).

5 Wu, M. R., Jusiak, B. & Lu, T. K. Engineering advanced cancer therapies with synthetic biology. *Nat Rev Cancer* **19**, 187-195, doi:10.1038/s41568-019-0121-0 (2019).

6 Gordon, M. G. *et al.* lentiMPRA and MPRAflow for high-throughput functional characterization of gene regulatory elements. *Nat Protoc* **15**, 2387-2412, doi:10.1038/s41596-020-0333-5 (2020).

7 Liu, Y. *et al.* Functional assessment of human enhancer activities using whole-genome STARR-sequencing. *Genome Biol* **18**, 219, doi:10.1186/s13059-017-1345-5 (2017).

8 Agarwal, V. *et al.* Massively parallel characterization of transcriptional regulatory elements. *Nature* **639**, 411-420, doi:10.1038/s41586-024-08430-9 (2025).

9 Fromel, R. *et al.* Design principles of cell-state-specific enhancers in hematopoiesis. *Cell* **188**, 3202-3218 e3221, doi:10.1016/j.cell.2025.04.017 (2025).

10 Kosicki, M. *et al.* Massively parallel reporter assays and mouse transgenic assays provide correlated and complementary information about neuronal enhancer activity. *Nat Commun* **16**, 4786, doi:10.1038/s41467-025-60064-1 (2025).

11 Mauduit, D. *et al.* Analysis of long and short enhancers in melanoma cell states. *ELIFE* **10**, doi:10.7554/eLife.71735 (2021).

12 de Almeida, B. P. *et al.* Targeted design of synthetic enhancers for selected tissues in the Drosophila embryo. *Nature* **626**, 207-211, doi:10.1038/s41586-023-06905-9 (2024).

13 Gosai, S. J. *et al.* Machine-guided design of cell-type-targeting cis-regulatory elements. *Nature* **634**, 1211-1220, doi:10.1038/s41586-024-08070-z (2024).

14 Taskiran, II *et al.* Cell-type-directed design of synthetic enhancers. *Nature* **626**, 212-220, doi:10.1038/s41586-023-06936-2 (2024).

15 Spitz, F. & Furlong, E. E. Transcription factors: from enhancer binding to developmental control. *Nat Rev Genet* **13**, 613-626, doi:10.1038/nrg3207 (2012).

16 Lambert, S. A. *et al.* The Human Transcription Factors. *Cell* **172**, 650-665, doi:10.1016/j.cell.2018.01.029 (2018).

17 Wu, M. R. *et al.* A high-throughput screening and computation platform for identifying synthetic promoters with enhanced cell-state specificity (SPECS). *Nat Commun* **10**, 2880, doi:10.1038/s41467-019-10912-8 (2019).

18 Georgakopoulos-Soares, I. *et al.* Transcription factor binding site orientation and order are major drivers of gene regulatory activity. *Nat Commun* **14**, 2333, doi:10.1038/s41467-023-37960-5 (2023).

19 MotifDb: An Annotated Collection of Protein-DNA Binding Sequence Motifs v. 1.50.0 (Bioconductor, 2025).

20 Reddy, J. *et al.* Predicting master transcription factors from pan-cancer expression data. *Sci Adv* **7**, eabf6123, doi:10.1126/sciadv.abf6123 (2021).

21 D'Alessio, A. C. *et al.* A Systematic Approach to Identify Candidate Transcription Factors that Control Cell Identity. *Stem Cell Reports* **5**, 763-775, doi:10.1016/j.stemcr.2015.09.016 (2015).
22 Kribelbauer-Swietek, J. F. *et al.* Context transcription factors establish cooperative environments and mediate enhancer communication. *Nat Genet* **56**, 2199-2212, doi:10.1038/s41588-024-01892-7 (2024).
23 Burgess, D. J. Regulatory elements: Putting enhancers into context. *Nat Rev Genet* **17**, 377, doi:10.1038/nrg.2016.74 (2016).
24 Cheng, J. K. & Alper, H. S. Transcriptomics-Guided Design of Synthetic Promoters for a Mammalian System. *ACS Synth Biol* **5**, 1455-1465, doi:10.1021/acssynbio.6b00075 (2016).
25 Shin, H. Y. *et al.* Establishment of five immortalized human ovarian surface epithelial cell lines via SV40 T antigen or HPV E6/E7 expression. *PLoS One* **13**, e0205297, doi:10.1371/journal.pone.0205297 (2018).
26 Zhu, B. *et al.* Synthetic biology approaches for improving the specificity and efficacy of cancer immunotherapy. *Cell Mol Immunol* **21**, 436-447, doi:10.1038/s41423-024-01153-x (2024).
27 Sadowski, I., Ma, J., Triezenberg, S. & Ptashne, M. GAL4-VP16 is an unusually potent transcriptional activator. *Nature* **335**, 563-564, doi:10.1038/335563a0 (1988).
28 Reinke, A. W., Grant, R. A. & Keating, A. E. A synthetic coiled-coil interactome provides heterospecific modules for molecular engineering. *J Am Chem Soc* **132**, 6025-6031, doi:10.1021/ja907617a (2010).
29 Das, A. T., Tenenbaum, L. & Berkhout, B. Tet-On Systems For Doxycycline-inducible Gene Expression. *Curr Gene Ther* **16**, 156-167, doi:10.2174/1566523216666160524144041 (2016).
30 Iyer, S. *et al.* Genetically Defined Syngeneic Mouse Models of Ovarian Cancer as Tools for the Discovery of Combination Immunotherapy. *Cancer Discov* **11**, 384-407, doi:10.1158/2159-8290.CD-20-0818 (2021).
31 Anderson, K. G., Stromnes, I. M. & Greenberg, P. D. Obstacles Posed by the Tumor Microenvironment to T cell Activity: A Case for Synergistic Therapies. *Cancer Cell* **31**, 311-325, doi:10.1016/j.ccell.2017.02.008 (2017).
32 Raskov, H., Orhan, A., Christensen, J. P. & Gogenur, I. Cytotoxic CD8(+) T cells in cancer and cancer immunotherapy. *Br J Cancer* **124**, 359-367, doi:10.1038/s41416-020-01048-4 (2021).
33 Zhou, S. J., Liu, M. G., Ren, F., Meng, X. J. & Yu, J. M. The landscape of bispecific T cell engager in cancer treatment. *BIOMARKER RESEARCH* **9**, doi:10.1186/s40364-021-00294-9 (2021).
34 Liao, K. W. *et al.* Stable expression of chimeric anti-CD3 receptors on mammalian cells for stimulation of antitumor immunity. *Cancer Gene Ther* **10**, 779-790, doi:10.1038/sj.cgt.7700637 (2003).
35 Powell, M. D., Read, K. A., Sreekumar, B. K., Jones, D. M. & Oestreich, K. J. IL-12 signaling drives the differentiation and function of a T(H)1-derived T(FH1)-like cell population. *Sci Rep* **9**, 13991, doi:10.1038/s41598-019-50614-1 (2019).
36 Salmon, H. *et al.* Expansion and Activation of CD103+ Dendritic Cell Progenitors at the Tumor Site Enhances Tumor Responses to Therapeutic PD-L1 and BRAF Inhibition. *IMMUNITY* **44**, 924-938, doi:10.1016/j.immuni.2016.03.012 (2016).

37 Lin, Y., Sharma, S. & John, M. S. CCL21 Cancer Immunotherapy. *Cancers (Basel)* **6**, 1098-1110, doi:10.3390/cancers6021098 (2014).
38 Chen, R., Zou, J., Liu, J., Kang, R. & Tang, D. DAMPs in the immunogenicity of cell death. *Mol Cell* **85**, 3874-3889, doi:10.1016/j.molcel.2025.09.007 (2025).
39 Patel, S. A. & Minn, A. J. Combination Cancer Therapy with Immune Checkpoint Blockade: Mechanisms and Strategies. *IMMUNITY* **48**, 417-433, doi:10.1016/j.immuni.2018.03.007 (2018).
40 Han, J. *et al.* Long-acting IL-2 release from pressure-fused biomineral tablets promotes antitumor immune response. *Nat Cancer* **6**, 1384-1399, doi:10.1038/s43018-025-00993-4 (2025).
41 Kramer, E. D. & Abrams, S. I. Granulocytic Myeloid-Derived Suppressor Cells as Negative Regulators of Anticancer Immunity. *Front Immunol* **11**, 1963, doi:10.3389/fimmu.2020.01963 (2020).
42 Jeong, J., Suh, Y. & Jung, K. Context Drives Diversification of Monocytes and Neutrophils in Orchestrating the Tumor Microenvironment. *Front Immunol* **10**, 1817, doi:10.3389/fimmu.2019.01817 (2019).
43 Zhang, L. *et al.* Improving adoptive T cell therapy by targeting and controlling IL-12 expression to the tumor environment. *Mol Ther* **19**, 751-759, doi:10.1038/mt.2010.313 (2011).
44 Zhang, L. *et al.* Tumor-infiltrating lymphocytes genetically engineered with an inducible gene encoding interleukin-12 for the immunotherapy of metastatic melanoma. *Clin Cancer Res* **21**, 2278-2288, doi:10.1158/1078-0432.CCR-14-2085 (2015).
45 Liu, Y. *et al.* Armored Inducible Expression of IL-12 Enhances Antitumor Activity of Glypican-3-Targeted Chimeric Antigen Receptor-Engineered T Cells in Hepatocellular Carcinoma. *JOURNAL OF IMMUNOLOGY* **203**, 198-207, doi:10.4049/jimmunol.1800033 (2019).
46 Levine, B. L. *et al.* Gene transfer in humans using a conditionally replicating lentiviral vector. *Proc Natl Acad Sci U S A* **103**, 17372-17377, doi:10.1073/pnas.0608138103 (2006).
47 Scholler, J. *et al.* Decade-Long Safety and Function of Retroviral-Modified Chimeric Antigen Receptor T Cells. *SCIENCE TRANSLATIONAL MEDICINE* **4**, doi:10.1126/scitranslmed.3003761 (2012).
48 Teixeira, A. P. & Fussenegger, M. Synthetic Gene Circuits for Regulation of Next-Generation Cell-Based Therapeutics. *Adv Sci (Weinh)* **11**, e2309088, doi:10.1002/advs.202309088 (2024).
49 Inoue, F. & Ahituv, N. Decoding enhancers using massively parallel reporter assays. *Genomics* **106**, 159-164, doi:10.1016/j.ygeno.2015.06.005 (2015).
50 Lim, F. *et al.* Affinity-optimizing enhancer variants disrupt development. *Nature* **626**, 151-159, doi:10.1038/s41586-023-06922-8 (2024).
51 Kheradpour, P. & Kellis, M. Systematic discovery and characterization of regulatory motifs in ENCODE TF binding experiments. *Nucleic Acids Res* **42**, 2976-2987, doi:10.1093/nar/gkt1249 (2014).

Method

TREND library construction

For the generation of the TREND library, we collected PPMs for all human transcription factors from the Bioconductor MotifDb package (v1.46.0) and PWMs from the ENCODE motif compendium[51]. MotifDb aggregates experimentally determined transcription factor binding profiles derived from SELEX, HT-SELEX, protein-binding microarray (PBM), and ChIP-seq assays across major databases including JASPAR, UniPROBE, hPDI, ScerTF, Stamlab, and cisBP. The ENCODE dataset provided complementary PWMs inferred from large-scale ChIP-seq data across hundreds of transcription factors.

From each matrix, we generated a consensus motif and nine high-probability sequence variants, corresponding to the most likely transcription factor binding sequences derived from nucleotide probabilities within the matrix. Each motif was repeated in tandem with 3 bp spacers between adjacent sites until the total length of the variable region approached 129 bp, ensuring consistent construct size. All variable regions were synthesized as a pooled oligonucleotide library (oligopool) by Agilent Technologies, Inc. (Santa Clara, CA, USA) using array-based DNA synthesis. Each design in the pool contained a variable region comprising tandem transcription factor binding site repeats, flanked by constant elements including universal primer sites and restriction enzyme sites. Each oligonucleotide was then amplified by PCR using primers containing 20 bp random sequences, introducing a unique barcode for quantifying barcode abundance at both the DNA and RNA levels.

The barcode-containing fragments were first digested with AgeI and SbfI and cloned into a lentiviral backbone, generating an intermediate vector. This intermediate construct was then digested again with AscI and BamHI to insert the adenoviral minimal promoter and EGFP reporter gene, yielding the final expression cassette. In this configuration, each enhancer variant regulates EGFP expression, while its associated barcode is positioned at the 3′ end of the EGFP transcript, allowing quantification of barcode abundance at both the DNA and RNA levels. This design enabled quantitative assessment of enhancer activity through barcode-linked expression analysis.

SYNZIP library construction

The Zipper library was designed to systematically evaluate pairwise interactions among 55 synthetic coiled-coil "zipper" domains. All possible 55 × 55 zipper pairs were synthesized as an oligonucleotide pool in the format $zipper_1$-P2A-$zipper_2$, where the self-cleaving P2A peptide separates the two coding sequences. The oligonucleotide pool was synthesized by Agilent Technologies, Inc. (Santa Clara, CA, USA) using array-based DNA synthesis. The synthesized fragments were PCR-amplified and cloned into a GAL4-responsive expression vector containing the GAL4 promoter, such that each fragment was inserted between GAL4BD and VP16AD to generate the fusion construct GAL4BD-$zipper_1$-P2A-$zipper_2$-VP16AD. This configuration allows co-expression of paired zipper domains within the same cell under control of the GAL4 promoter, enabling high-throughput functional screening of zipper-zipper interactions.

Cell culture and cell lines

The human ovarian carcinoma cell line OV8 was originally established at the National Cancer Institute (NCI) and obtained from existing laboratory stocks. BPPNM, KPCA, and PPNM cell lines were gifts from the laboratory of Robert A. Weinberg (Massachusetts Institute of Technology). The ID8 murine ovarian cancer cell line was a gift from the laboratory of Katherine F. Roby (University of Kansas Medical Center). Lenti-X HEK293T (Takara, 632180), CCD-841 CoN cells (American Type Culture Collection, CRL-1790), IOSE (Applied Biological Materials, T1074), and OVCAR8 were cultured in DMEM (Corning, 10-013-CV) supplemented with 10% fetal bovine serum (FBS; Corning, 35-010-CV), 1% non-essential amino acids (MEM/NEAA; Hyclone, 16777-186), and 1% penicillin–streptomycin (Life Technologies, 15140-122). ID8 cells were cultured in DMEM supplemented with 10% heat-inactivated FBS and 1% penicillin–streptomycin. BPPNM, PPNM, and KPCA cells were cultured in DMEM supplemented with 1% insulin–transferrin–selenium (Thermo Fisher Scientific, 41400045), 2 ng/mL EGF (Life Technologies, PMG8041), 4% heat-inactivated FBS, and 1% penicillin–streptomycin. All cells were maintained at 37 °C in a humidified atmosphere containing 5% CO_2 and were routinely tested negative for mycoplasma contamination.

Primary human T cells

Leukoreduction collars from anonymous healthy platelet donors were obtained through the Brigham and Women's Hospital Crimson Core Laboratory. $CD3^+$ T cells were isolated from the

white blood cell fraction using the RosetteSep Human T Cell Enrichment Kit (STEMCELL Technologies, 15021), followed by density gradient centrifugation with Lymphocyte Separation Medium (Corning, 25-072-CV) and SepMate-50 tubes (STEMCELL Technologies, 85450).

Lentivirus Production and Transduction

Lentiviral particles were generated by reverse transfection of HEK293T cells in a 24-well format using FuGENE-HD (Promega, E2311). All plasmid DNA was normalized to 0.1 µg/µl in sterile water. For each well, a plasmid mixture containing 0.2 µg of lentiviral transfer vector, 0.1 µg psPAX2 (Addgene #12260), and 0.1 µg pVSV-G (Addgene #138479) was prepared. In parallel, 2.4 µl of FuGENE-HD was diluted in 20 µl of Opti-MEM (Thermo Fisher Scientific, 31985070), mixed with the plasmid solution, vortexed briefly, and incubated at room temperature for 15-20 min to allow complex formation.

HEK293T cells were maintained below 80% confluency, and the culture medium was replaced with fresh DMEM 2-4 hours before transfection to promote optimal viral yield. Cells were trypsinized, counted, and resuspended in DMEM to a final concentration of 3.6×10^6 cells/mL. A volume of 100 µl of the cell suspension (3.6×10^5 cells) was added to each transfection tube containing the FuGENE-DNA complexes, mixed gently, and plated into wells pre-filled with 300 µl of fresh DMEM. Eighteen to twenty hours after transfection, the medium was replaced with 500 µl of fresh DMEM. Viral supernatants were harvested 44-48 hours post-transfection, clarified by centrifugation, and filtered through a 0.45 µm syringe filter (Pall Corporation, 4614). Filtered lentivirus was used immediately or stored at 4 °C for up to 3 days or -80 °C for long-term storage.

For transduction, 1.25×10^6 target cells were infected with serial dilutions of filtered viral supernatant in the presence of 8 µg/mL polybrene (Sigma) overnight. Medium was replaced the following day. For comparative experiments, viral titers were normalized using the Lenti-X p24 Rapid Titer Kit (Takara, 631476) before use.

Inducible transcription factor overexpression and reporter assay

A doxycycline-inducible (Tet-On) system was used to regulate TF expression in IOSE cells. IOSE cells were co-infected with three lentiviral vectors: one encoding the reverse tetracycline-controlled transactivator 3 (rtTA3) under the UbC promoter, a second encoding doxycycline-inducible MYC or E2F4 (Tet-On system), and a third carrying the synthetic enhancer-driven EGFP

reporter (MYC_v4 or E2F_v2). Seventy-two hours after infection, cells were treated with increasing concentrations of doxycycline (0, 100, and 1000 ng/mL; Thermo Scientific Chemicals, J60579) for 72 hours to induce graded TF expression. Reporter activity was quantified by flow cytometry (Beckman Coulter, CytoFLEX), and median EGFP fluorescence intensity was analyzed using FlowJo software.

T cell activation and transduction

Cryopreserved primary human T cells were thawed (day 0) and cultured in RPMI 1640 (Corning, 10-040-CV) supplemented with 10% heat-inactivated FBS, 10 mM HEPES (Life Technologies, 15630080), 0.1 mM NEAA, 1 mM sodium pyruvate (Life Technologies, 11360-070), 1% penicillin–streptomycin, 50 μM 2-mercaptoethanol (Sigma-Aldrich, M3148-25ML), and 50 IU/mL recombinant human IL-2 (NCI). T cells were stimulated using the Human CD3/CD28 T Cell Activator (STEMCELL Technologies, 10971) according to the manufacturer's protocol. On day 2, activated T cells were resuspended in lentiviral supernatant and centrifuged at 2,000 × g for 2 h at 32 °C (spinoculation). Viral supernatants were then replaced with fresh culture medium. After transduction, T cells were maintained by diluting 1:2 daily with fresh medium to sustain exponential growth and viability.

For screening and validation of synthetic enhancers, T cells were transduced on day 2 and cultured as described above. On day 10, cells were restimulated with the Human CD3/CD28 T Cell Activator and collected 24 hours later for analysis.

Lentiviral library transduction and sequencing

Pooled lentiviral libraries, including the TREND and Zipper constructs, were packaged and transduced into the respective target cell types using the standard lentiviral production and transduction workflow described above. To ensure reproducibility and minimize sampling bias, we maintained >100-fold representation of each library element throughout the screening pipeline. Five days post-transduction, genomic DNA and total RNA were isolated from pooled cell populations using the AllPrep DNA/RNA Mini Kit (Qiagen, 80204).

DNA library preparation: Barcoded genomic DNA fragments were first amplified by a limited-cycle PCR (3 cycles) using primers that introduced unique molecular identifiers (UMIs), sample indices, and Illumina adapter sequences, enabling simultaneous UMI tagging and adapter

addition while minimizing amplification bias. The resulting products were then amplified in a second PCR (15 cycles) using universal Illumina primers to enrich adapter-ligated fragments and generate sequencing-ready libraries. Amplicons of the expected size (~132 bp) were gel-purified, pooled, and cleaned prior to sequencing.

RNA library preparation: For each sample, 2 µg of total RNA was reverse-transcribed using primers containing a 5′ Illumina adapter, a unique molecular identifier (UMI), and a sample-specific index sequence. Reverse transcription was performed at 42 °C for 60 min, followed by heat inactivation at 85 °C for 5 min. After RNase A treatment, cDNA was amplified by PCR (~15 cycles) using Illumina-compatible universal primers to generate sequencing-ready amplicons (~132 bp). Where indicated, emulsion PCR was tested using Q5 polymerase supplemented with 0.02 mg/mL BSA to reduce amplification bias.

Sequencing libraries were quantified, pooled, and sequenced at the Dana-Farber Cancer Institute Molecular Biology Core Facility on an Illumina NovaSeq platform using 150 bp paired-end reads.

Barcode quantification and enhancer activity analysis

Sequencing data were processed using a custom in-house pipeline implemented on the Harvard Medical School O2 high-performance computing cluster. Read orientation ("flipping") and sample demultiplexing were performed using in-house Python scripts guided by predefined barcode–sample key tables. Demultiplexed reads were collapsed using FASTX-Toolkit (fastx_collapser) to remove duplicate reads, and the resulting files were aligned to the reference library using Bowtie2 with parameters optimized for short, high-similarity sequences. Barcode sequences were then extracted from read pairs using in-house Python and R scripts, and identical barcodes were aggregated to minimize PCR and sequencing biases. Aligned reads were processed with SAMtools to obtain barcode-level count tables for DNA and RNA libraries.

Downstream analysis was performed using an in-house R script. Barcodes with zero DNA or RNA counts were excluded, and constructs represented by fewer than a specified minimal number of independent barcodes were filtered out to ensure reproducibility. For each barcode, the RNA/DNA ratio was calculated as a quantitative measure of enhancer activity. Within each biological replicate, barcode-level ratios were summarized by their median value, and the mean of these replicate medians was used to represent the final enhancer activity score for each construct.

To ensure quantitative robustness, we examined the distribution of DNA barcode for each sample and defined a lower DNA-abundance threshold such that at least 75% of constructs (cancer-specific enhancer project) or 50% of constructs (activation-specific enhancer project) remained transcriptionally active above that cutoff. Barcodes passing this threshold were aggregated by enhancer identity, and constructs meeting coverage criteria were retained for downstream analysis. These activity scores were then used for comparative analysis between tumor and control cell lines or between activated and resting T-cell states. For the cancer-specific enhancer validation experiments, top candidates were selected based on consistent performance across biological replicates. For the activation-specific enhancer validation, top candidates were prioritized from the full library screen in individual donors, with additional preference given to enhancers containing motifs derived from FOS, AP-1, or NFAT families.

Bulk RNA-seq analysis

Total RNA from OV8 and IOSE cells was extracted and submitted to Azenta Life Sciences (GENEWIZ, South Plainfield, NJ, USA) for library preparation and sequencing. RNA quantity was measured using a Qubit 2.0 Fluorometer (Thermo Fisher Scientific), and RNA integrity was assessed with an Agilent TapeStation 4200 (Agilent Technologies). RNA-seq libraries were prepared using the NEBNext Ultra II RNA Library Prep Kit for Illumina (New England Biolabs) with poly(A) selection, following the manufacturer's protocol. Briefly, mRNA was enriched using Oligo(dT) beads, fragmented at 94 °C for 15 min, and reverse-transcribed to generate first- and second-strand cDNA. The resulting cDNA fragments were end-repaired, adenylated at the 3′ ends, ligated to Illumina adapters, and amplified by limited-cycle PCR. Library size and concentration were verified using the Agilent TapeStation and Qubit fluorometer.

Sequencing was performed on an Illumina NovaSeq 6000 platform in a 2 × 150 bp paired-end configuration, targeting approximately 30 million reads per sample. Raw sequencing data were converted to FASTQ format and demultiplexed using bcl2fastq v2.20, allowing one mismatch for index recognition. Adapter trimming and quality filtering were performed with Trimmomatic v0.36. Clean reads were aligned to the human reference genome (ENSEMBL) using STAR v2.5.2b, and gene-level read counts were generated with featureCounts v1.5.2 from the Subread package, considering only uniquely mapped reads within annotated exon regions. Transcript abundance was normalized as TPM for downstream analysis.

Animal experiments

All animal care and experiments were conducted at the Dana-Farber Cancer Institute Animal Research Facility under protocol 19-014, reviewed and approved by the Institutional Animal Care and Use Committee. Mice were housed in ventilated cages (up to five mice per cage) under standard conditions including controlled light/dark cycles, temperature, and humidity.

In vivo antitumor efficacy validation

Three million BPPNM cells engineered to stably express firefly luciferase (BPPNM-Luc) were suspended in a 1:1 mixture of Matrigel (Corning, 47743-710) and phosphate-buffered saline (PBS) and injected intraperitoneally into 6-8-week-old female C57BL/6 mice (Jackson Laboratory, 000664). Tumor progression was monitored by bioluminescence imaging using an IVIS Spectrum imaging system (Xenogen), and images were analyzed with Living Image Software v4.7.4. On day 6 post-implantation, mice were imaged to assess baseline tumor burden; animals showing outlier radiance values were excluded to minimize bias. The remaining mice with comparable radiance levels were then randomly assigned to experimental groups.

For in vivo delivery of the S8IP circuit, lentiviruses encoding each circuit component (module 1, module 2, STE, CD80, IL12, and anti-PD1 antibody) were produced as described above and concentrated tenfold using a Sorvall WX 80+ ultracentrifuge. Concentrated lentiviruses were combined at a volume ratio of module 1 : module 2 : STE : CD80 : IL12 : anti-PD1 = 1 : 1 : 0.5 : 0.5 : 0.5 : 0.5. Lentiviruses for other circuit groups, including SCIP, S8FP, SFIP, S8GP, and SFGP were produced using the same method. Each mouse received an intraperitoneal injection of 400 μL of the viral mixture (~1×10^{10} viral particles/mL), while the higher-dose group received 400 μL at approximately 2×10^{10} viral particles/mL. For control groups, lentiviruses were mixed at identical ratios, substituting the S8IP components with vectors encoding the output reporter rtTA3 or PBS. Viral titers were quantified and normalized before injection using the Lenti-X p24 Rapid Titer Kit (Takara, 631476).

Flow cytometry for immune analysis

BPPNM tumor-bearing mice received an intraperitoneal injection of the S8IP circuit at a dose of 400 μL of viral mixture (~2×10^{10} viral particles/mL) on day 14 after tumor inoculation. Peritoneal

wash was collected 7 days later for analysis. Briefly, mice were euthanized and injected with 5 mL of cold PBS to collect the peritoneal fluid. The collected fluid was centrifuged at 800 x g for 5 min at 4 °C, and the cell pellet was subjected to red blood cell lysis with ACK buffer for 10 min at room temperature. After washing with PBS, cells were resuspended in FACS buffer and passed through 70-μm strainers prior to downstream applications.

For surface staining, cells were first incubated with TruStain FcX™ PLUS (BioLegend, 156603) for 10 min on ice, followed by staining with fluorophore-conjugated antibodies (1:200 dilution, 30 min at 4 °C). After washing with PBS, cells were incubated with Zombie NIR viability dye (BioLegend, 423105; 1:1000 in PBS) for 30 min at 4 °C.

Antibodies used for lymphoid cell analysis include BUV737-CD3 (BD Biosciences, 612821), BV510-CD45 (BioLegend, 103137), BV650-CD4 (BioLegend, 100545), BV711-CD8 (BioLegend, 100747), BV785-CD62L (BioLegend, 104440), Percp Cy5.5-TIM3 (BioLegend, 119717), PE-NK1.1 (BioLegend, 156503), PE/Dazzle 594-CD44 (BioLegend, 103055), PE-Cy7-CD19 (BioLegend, 115519), APC-PD1 (BioLegend, 135210), AF700-CD25 (BioLegend, 102024) and APC-Cy7-CD11b (BioLegend, 101225). APC-Cy7-CD11b was used to exclude $CD11b^+$ cells from lymphoid analysis.

Antibodies used for myeloid cell analysis include BV421-Ly6G (BioLegend, 127627), BV510-CD45 (BioLegend, 103137), BV650-CD11c (BioLegend, 117339), BV785-CD11b (BioLegend, 101243), Percp Cy5.5-Ly6C (BioLegend, 128011), PE-XCR1 (BioLegend, 148204), PE/Cy5-F4/80 (BioLegend, 123111), PE-Cy7-CD172a (BioLegend, 144007), APC-CD206 (BioLegend, 141708), AF700-MHCII (BioLegend, 107621), APC-Cy7-CD3 (BioLegend, 100221) and APC-Cy7-CD19 (BioLegend, 115529). APC-Cy7-CD3 and APC-Cy7-CD19 were used to exclude $CD3^+$ cells and $CD19^+$ cells from myeloid analysis.

For intracellular staining, cells were stimulated in culture at 1×10^6 cells/mL with 2 μl/mL of activation cocktail and GolgiPlug (BD Biosciences, 550583) for 4 h at 37 °C. Cells were washed once and pre-incubated with TruStain FcX™ PLUS for 10 min on ice, followed by surface antibody staining (1:200, 30 min at 4 °C) and Zombie NIR staining (1:1000, 20 min in PBS). After PBS wash, cells were then fixed and permeabilized using the FoxP3/Transcription Factor Staining Buffer Set (eBioscience, 00-5523-00), washed twice with permeabilization buffer, and incubated with intracellular antibodies (1:100 in permeabilization buffer, 1 h at room temperature).

Antibodies used for intracellular cytokines analysis include BUV737-CD3 (BD Biosciences, 612821), BV421-granzyme B (BioLegend, 515409), BV510-CD45 (BioLegend, 103137), BV650-CD4 (BioLegend, 100545), BV711-CD8 (BioLegend, 100747), BV785-IFN-γ (BioLegend, 505838), PE-Perforin (ebioscience, 12-9392-82), PE-Cy7-NK1.1 (BioLegend, 156513), APC-IL-4 (BioLegend, 504105), AF700-Foxp3 (BioLegend, 126421) and APC-Cy7-CD11b (BioLegend, 101225).

Samples were acquired with Cytek Aurora using SpectroFlo v.3.1.0. Collected data were analysed using FlowJo v.10.8.1 Software.

In vivo specificity validation

Three million BPPNM cells were resuspended in a 1:1 mixture of Matrigel (Corning, 47743-710) and PBS and injected intraperitoneally into 6–8-week-old female C57BL/6 mice (Jackson Laboratory). On day 6 post-tumor implantation, mice received 400 μL of lentivirus (~2×10^{10} viral particles/mL) encoding firefly luciferase driven by synthetic enhancers. Luciferase activity was measured on day 18 by in vivo bioluminescence imaging using an IVIS Spectrum imaging system (Xenogen), and analyzed with Living Image Software v4.7.4.

For AND-gate and CMV control groups, lentiviruses were concentrated tenfold using a Sorvall WX 80+ ultracentrifuge and mixed at a volume ratio of module 1 : module 2 : luciferase = 1 : 1 : 2. On day 6, each mouse was administered 400 μL of the viral mixture (~2×10^{10} viral particles/mL) or lentivirus encoding luciferase under the CMV promoter. On day 28, the liver, kidney, spleen, intestine, peritoneal wall, and tumor tissues were harvested for ex vivo bioluminescence imaging.

Statistical analysis

Data were analyzed using GraphPad Prism v10.4.1. The statistical tests applied to each dataset are specified in the corresponding figure legends. Unless otherwise noted, values are presented as mean ± s.e.m. Statistical significance was assessed using unpaired two-tailed Student's t-tests, log-rank (Mantel-Cox) test, one-way analysis of variance (ANOVA) or two-way ANOVA followed by Tukey's multiple comparisons test. Statistical difference was considered significant at *$P < 0.05$, **$P < 0.01$, ***$P < 0.001$. **** $P < 0.0001$.

Materials availability

The TREND library and key plasmids generated in this study will be deposited in Addgene upon publication. Other materials are available from the corresponding author upon reasonable request.

Code and data availability

Processed sequencing data, including post-alignment RNA and DNA barcode count tables for all screens, and summarized screening results will be made available upon publication. The accompanying R scripts for enhancer activity quantification (barcode filtering, normalization, and activity scoring) will be made available alongside the processed data. Raw sequencing data are available from the corresponding author upon reasonable request, in accordance with institutional data-sharing policies.

Acknowledgements

We thank the Molecular Biology Core Facility (MBCF) at Dana-Farber Cancer Institute for technical support and the Animal Research Facility (ARF) for expert animal care. This work was supported by the Cancer Research Institute (CRI) CLIP Award, the Department of Defense Ovarian Cancer Research Program (OC220238/W81XWH-22-OCRP-IIRA), and the Parker Institute for Cancer Immunotherapy.

Author contributions

Y.J., C.-Y.C., and M.-R.W. conceived the study and developed the methodology. Y.J. and M.-R.W. analyzed and interpreted the data and wrote the manuscript. Y.J., C.-Y.C., B.Z., R.W., A.M.S., S.H., Y.-N.L., H.Y., T.S., Y.-C.W. and Z.W. performed experiments and collected data. L.S., Y.W. and E.B.A. provided technical support and contributed to data interpretation. M.-R.W. supervised the study and coordinated the overall project.

Competing interests

The authors declare that they have submitted patent applications related to the technology described in this study.

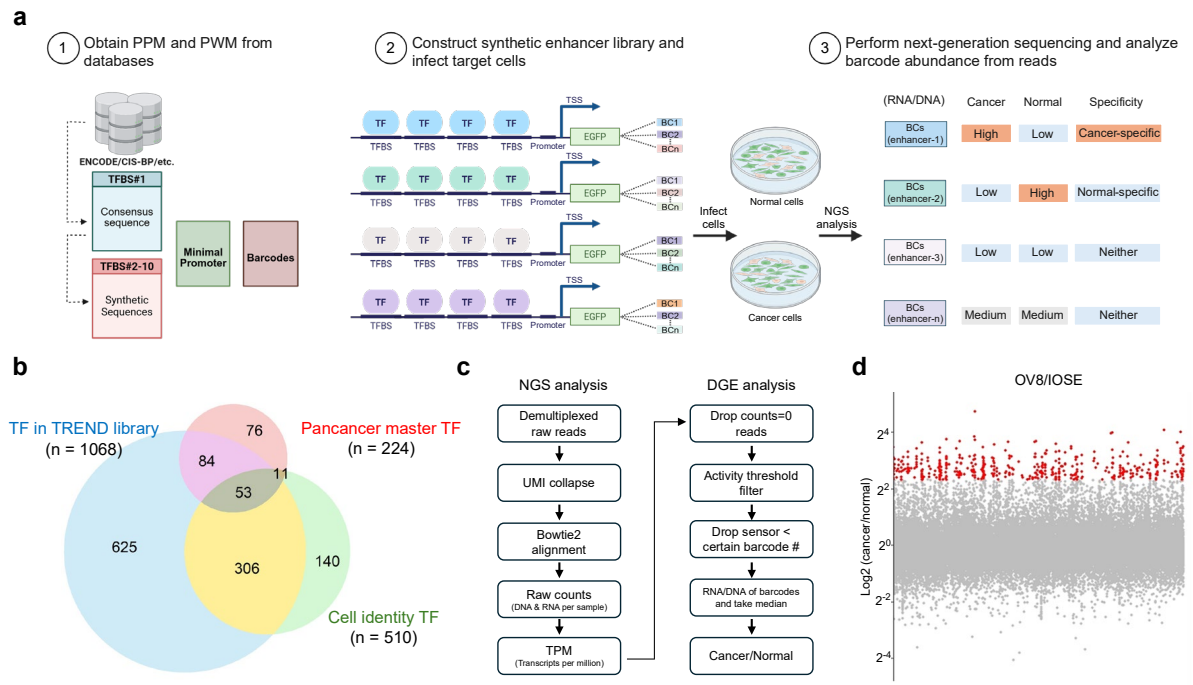

Fig. 1. TREND platform for high-throughput discovery of synthetic enhancers. a, Schematic of the TREND workflow for systematic identification of context-specific synthetic enhancers. (1) PPMs and PWMs for 1,068 TFs were obtained from 14 public databases (ENCODE, CIS-BP, etc.) to generate consensus motifs and the nine most probable sequence variants from each matrix. (2) Each motif or variant was concatenated in tandem upstream of an adenoviral minimal promoter and linked to unique DNA barcodes to create a pooled lentiviral library. The library was packaged and delivered into normal and cancer cells. (3) Barcode abundance in RNA and DNA was quantified by targeted NGS, and enhancer activity and specificity were inferred from RNA/DNA ratios across conditions. **b**, Venn diagram showing overlap of TFs represented in the TREND library with pan-cancer master regulators and cell-identity TF sets. **c,** Computational pipeline for TREND screening data processing, including demultiplexing, unique UMI collapsing, read alignment, normalization, and activity threshold filtering. **d**, Differential activity between ovarian cancer (OV8) and normal ovarian epithelial (IOSE) cells, highlighting cancer-selective synthetic enhancers (red) with high cancer-to-normal ratios.

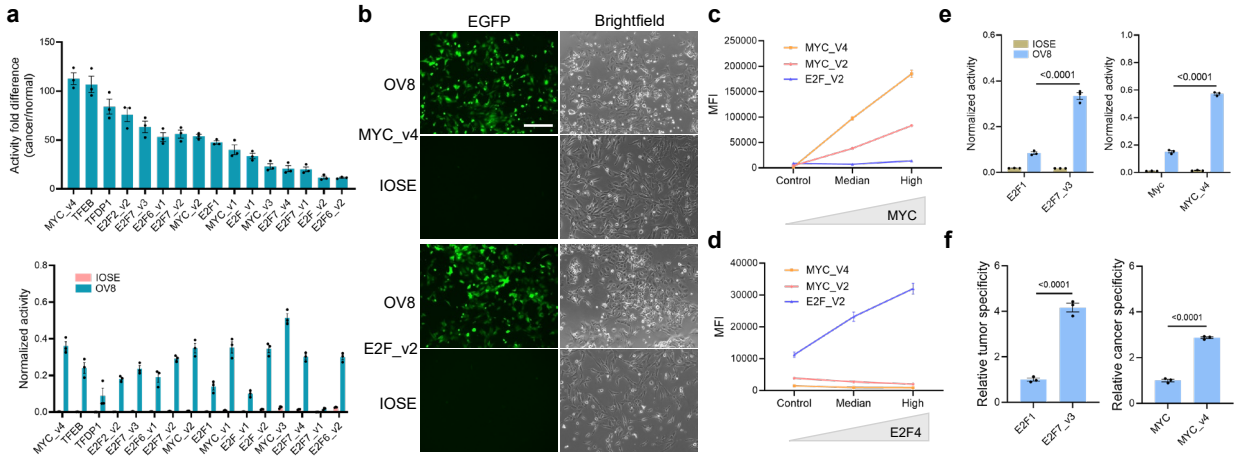

Fig. 2. Functional validation of cancer-selective synthetic enhancers identified by TREND. a, Quantitative reporter assays of individually cloned synthetic enhancers in human ovarian cancer (OV8) and normal ovarian epithelial (IOSE) cells measured by flow cytometry. Enhancer activity was normalized to the constitutive ubiquitin C (UbC) promoter control, and the activity fold difference was calculated as the ratio of normalized activity in OV8 cells relative to IOSE cells. v1, v2, v3, v4, etc. represent distinct motif variants derived from the same TF. **b,** Representative fluorescence microscopy images of OV8 and IOSE cells transduced with MYC_v4 or E2F_v2 synthetic enhancers driving EGFP expression. Scale bar, 200 µm. **c,d,** Reporter assays showing doxycycline dose-dependent activation of MYC_v4 and MYC_v2 (**c**) or E2F_v2 (**d**) enhancers following induction of their cognate TFs (MYC or E2F4) in IOSE cells. Data show median fluorescence intensity (MFI) of EGFP (n = 3) measured by flow cytometry. **e,f,** Comparison of TREND-derived synthetic enhancers with previously reported designs in OV8 cells. E2F7_v3 and MYC_v4 were identified by TREND, whereas E2F1 and MYC represent previously reported enhancers. **e**, Reporter activity driven by each enhancer. **f**, Relative cancer specificity calculated as the ratio of enhancer activity in OV8 versus IOSE cells, with values normalized to the previously reported E2F1 and Myc enhancers. Data are mean ± s.e.m. from three independent experiments. Statistical significance was determined by unpaired two-tailed Student's t-tests.

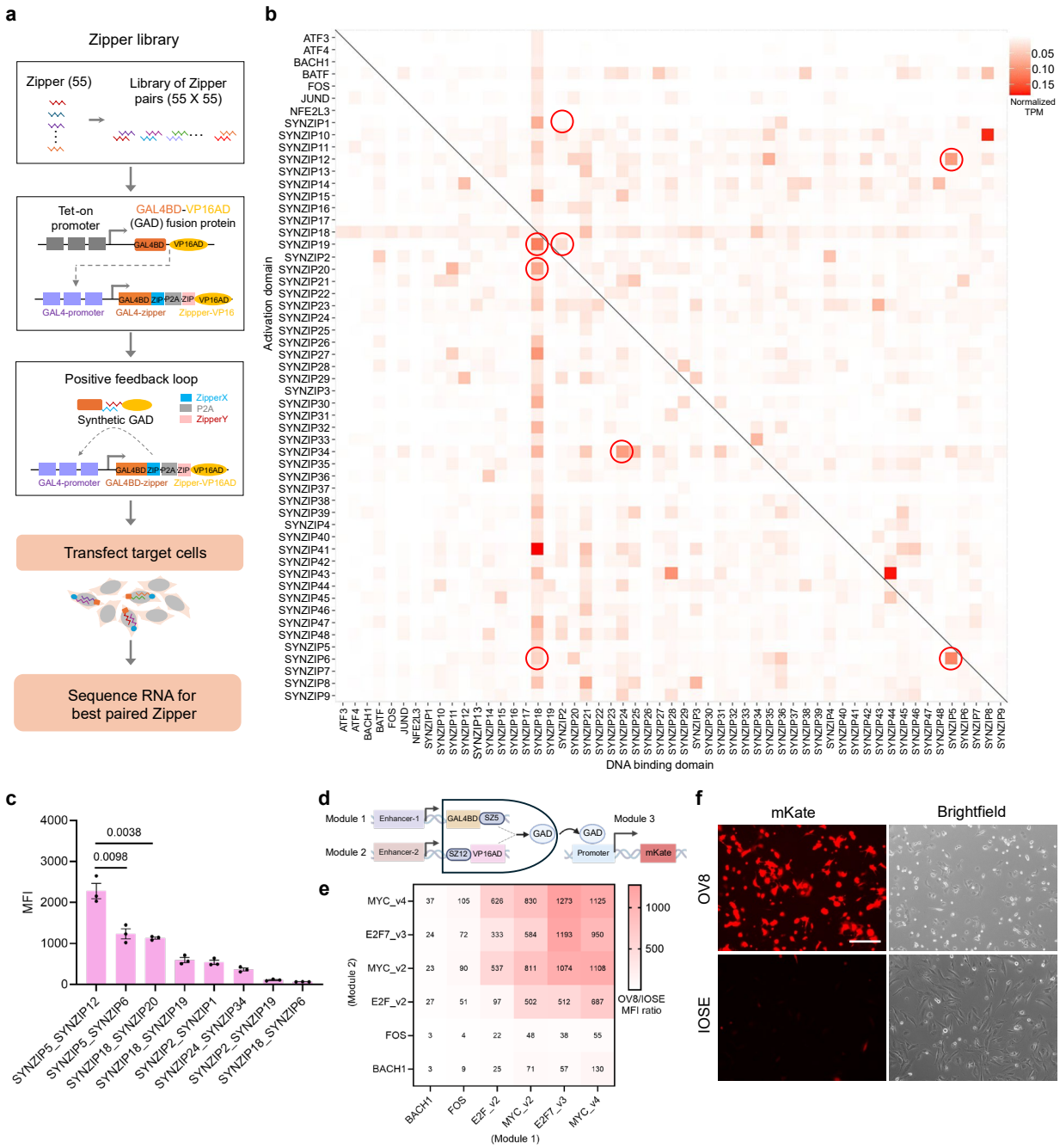

Fig. 3. Construction of enhancer-driven AND-gate circuits through coiled-coil–mediated protein interactions. a, Overview of the coiled-coil interaction screen used to identify optimal zipper pairs for circuit design. Each candidate coiled-coil domain was fused to either the GAL4BD-zipper or the zipper-VP16AD and expressed in HEK293T cells. Productive interactions between complementary zippers reconstitute a functional GAD, which drives reporter expression from a GAL4-responsive promoter. Transcript quantification by RNA sequencing was used to

identify the most efficient interacting pairs. **b,** Heatmap of pairwise interactions among 55 coiled-coil domain combinations, highlighting high-activity pairs (circled). **c,** Flow-cytometry analysis of reporter activity for selected zipper pairs in HEK293T cells. **d,** Schematic of the enhancer-driven AND-gate circuit, in which two distinct TREND enhancers independently drive GAL4BD-zipper and zipper-VP16AD expression. Productive coiled-coil pairing between the two proteins reconstitutes an active GAD complex, enforcing AND logic at the transcriptional level. **e,** Cancer-to-normal activity ratios of AND-gate constructs assembled from synthetic enhancers MYC_v4, E2F7_v3, MYC_v2, E2F_v2, FOS, and BACH1, showing varying degrees of cancer selectivity. Heatmap values represent the mean from three independent experiments**. f,** Representative fluorescence-microscopy images of mKate reporter in OV8 and IOSE cells transduced with the AND-gate construct. Scale bar, 200 μm. Data are mean ± s.e.m. from three independent experiments. Statistical significance was determined by unpaired two-tailed Student's t-tests.

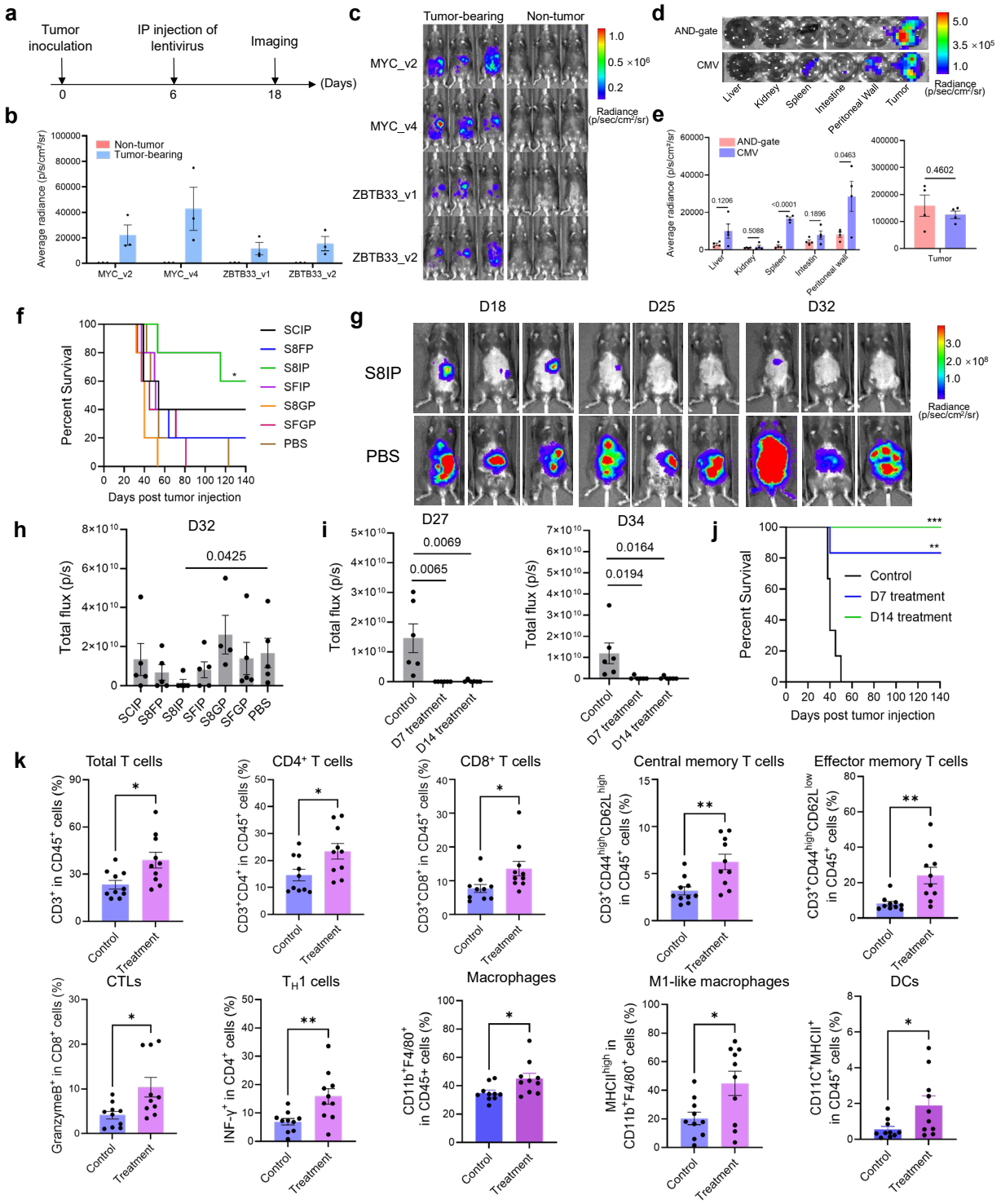

Fig. 4. Tumor-restricted AND-gate circuits reprogram the tumor microenvironment and elicit durable therapeutic responses in murine ovarian cancer. a, Experimental design for testing tumor specificity of individual TREND-derived synthetic enhancers in BPPNM tumor-bearing mice. **b,** Quantification of bioluminescence signals from tumor-bearing and tumor-free

mice (n = 3 mice per group). **c,** Representative bioluminescence images of mice bearing BPPNM tumors or tumor-free controls following transduction with luciferase driven by single synthetic enhancers. **d,** Ex vivo bioluminescence imaging of organs from mice transduced with enhancer-driven AND-gate circuits or CMV promoter-driven luciferase. **e,** Quantification of luciferase activity across major normal organs following delivery of AND-gate circuits or CMV enhancer constructs (n = 4 mice per group). **f,** Survival curves of BPPNM tumor-bearing mice treated with AND-gate circuits encoding different combinations of immune effectors (n = 5 per group). **g,** Representative bioluminescence images of tumor burden in treated mice. **h,** Quantification of tumor growth on day 32 based on bioluminescence imaging (n = 5 per group). **i,** Quantification of tumor growth in BPPNM tumor-bearing mice treated with a two-fold higher dose (relative to panels **f-h**) of the S8IP circuit, administered on day 7 or day 14 after tumor inoculation (n = 6 per group). **j,** Survival curves of mice treated with the S8IP circuit on day 7 or 14, showing prolonged survival with both early and delayed dosing (n = 6 per group). **k,** Flow-cytometry analysis of peritoneal immune cells following S8IP circuit treatment. BPPNM tumor-bearing mice were treated with the S8IP circuit at the dosage used in panels **i-j**, administered on day 14 after tumor inoculation. Peritoneal wash was collected 7 days later for analysis. n = 10 per group. Statistical significance was determined by unpaired two-tailed t-tests or log-rank (Mantel-Cox) test. *P < 0.05, **P < 0.01, ***P < 0.001 and ****P < 0.0001.

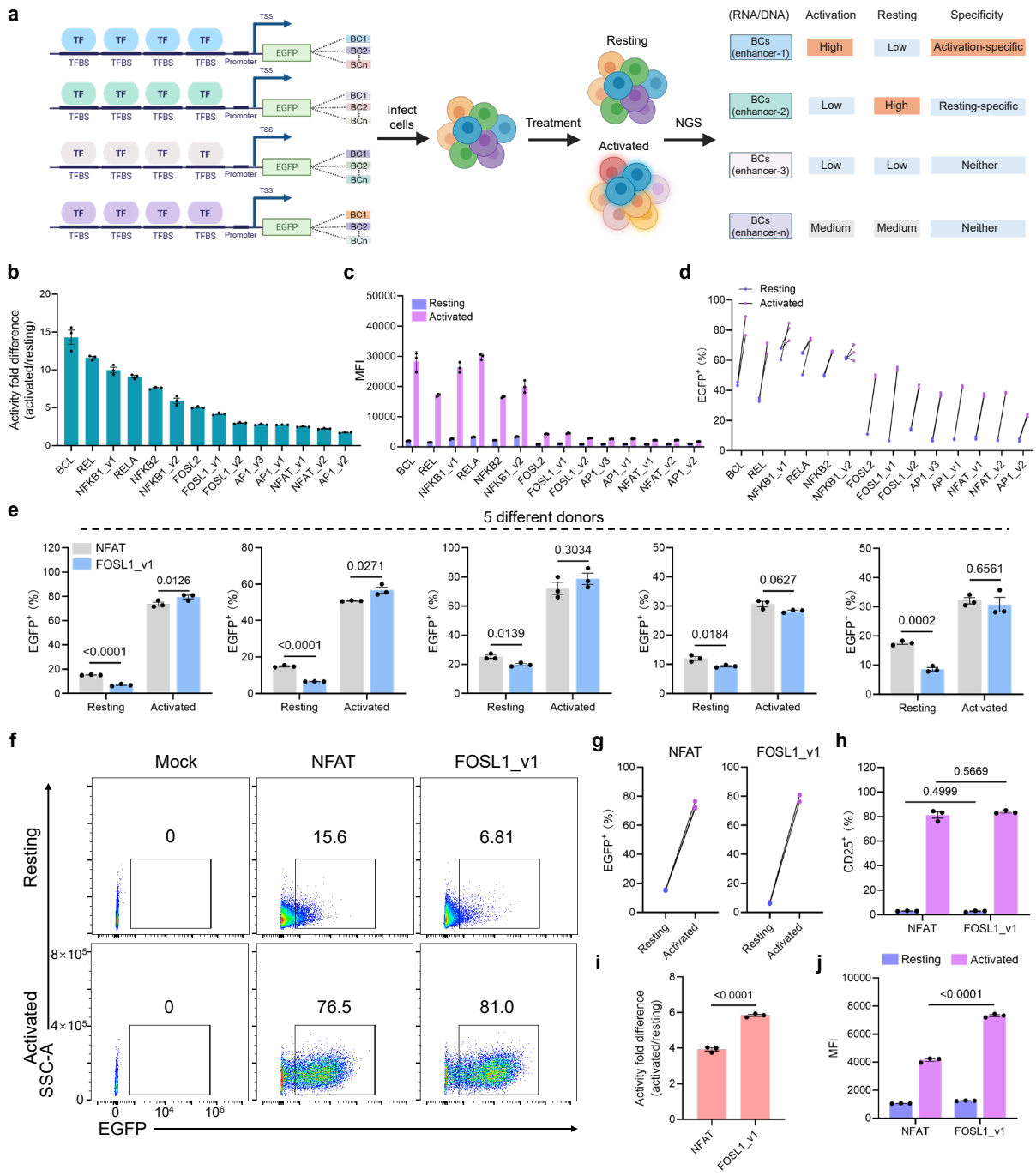

Fig. 5. Identification of activation-responsive synthetic enhancers in T cells using TREND. **a,** Schematic of the pooled screening workflow in human primary T cells. Cells were transduced with the TREND library, stimulated with anti-CD3/CD28 antibody, and enhancer activity was quantified by sequencing barcode-linked transcripts. **b,** Fold difference in reporter activity (activated relative to resting condition) for all tested enhancers, identifying candidates responsive to T cell activation. **c**, MFI of EGFP expression driven by individual enhancers in activated versus

resting T cells. **d,** Percentage of $EGFP^+$ T cells under activated and resting conditions, showing activation-induced enhancer responsiveness. **e,** Comparison of $EGFP^+$ cell percentages for the canonical NFAT-motif-based enhancer and the TREND-derived FOSL1_v1 enhancer under activated and resting conditions. **f,** Representative flow cytometry analysis showing EGFP expression driven by NFAT and FOSL1_v1 enhancers in resting and activated T cells. **g**, Quantification of $EGFP^+$ cell percentages from panel (**f**). **h**, Proportion of $CD25^+$ T cells transduced with NFAT or FOSL1_v1 enhancer under resting and activated conditions. **i**, Fold difference in reporter activity (activated relative to resting condition) for NFAT and FOSL1_v1 enhancers. **j**, MFI of EGFP expression for NFAT and FOSL1_v1 enhancers in activated and resting T cells. Data are mean ± s.e.m. from three independent experiments. Statistical significance was determined by unpaired two-tailed t-tests.

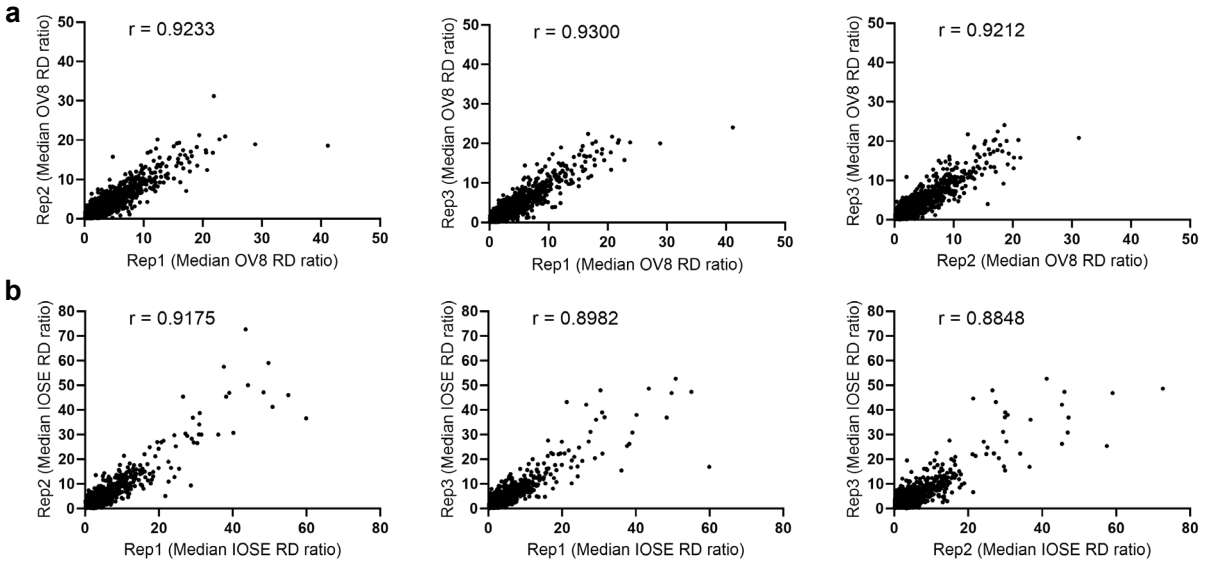

Extended Data Fig. 1. TREND screening shows high reproducibility across biological replicates. a,b, Correlation of synthetic enhancer activity profiles between independent biological screening replicates in OV8 **(a)** and IOSE **(b)** cells. Each point represents a synthetic enhancer, with RNA output normalized to DNA input (RNA/DNA ratio, referred to as RD ratio). Pearson correlation coefficients indicate high reproducibility between TREND screening replicates.

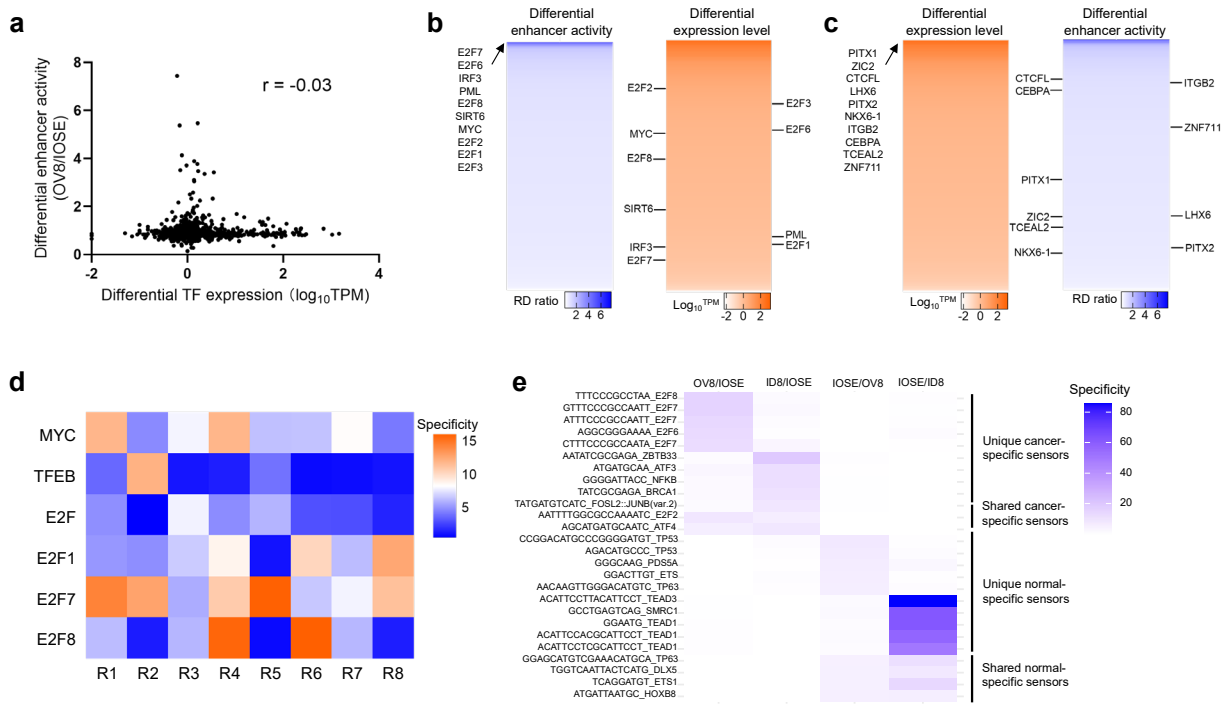

Extended Data Fig. 2. Relationship between TF abundance, motif variant rank, and synthetic enhancer activity. a, Scatterplot comparing differential TF mRNA expression (OV8 versus IOSE) with the corresponding differential activity (OV8 versus IOSE) of the synthetic enhancers responsive to each TF, measured by TREND. Each point represents a specific TF. **b,c,** Heatmaps comparing differential enhancer activity (OV8/IOSE activity ratio) of TREND-identified synthetic enhancers with the corresponding TF differential expression (OV8/IOSE, RNA-seq). TFs associated with top-performing cancer-specific enhancers are dispersed throughout the TF differential-expression landscape rather than concentrated among highly differentially expressed TFs **(b)**, and conversely, TFs with high transcript differences are distributed across a wide range of enhancer specificity without a consistent trend **(c)**. **d,** Heatmap showing the relationship between motif variant rank within the PPM and enhancer specificity across TFs. Highly cancer-specific enhancers can arise from any motif rank, whether consensus or lower-ranked variants, rather than clustering at a particular rank. **e,** TREND identified multiple classes of enhancers, including those selective for human cancer cells (OV8/IOSE-specific), mouse cancer cells (ID8/IOSE-specific), and shared cancer-selective elements active in both human and mouse cancer cells (OV8/IOSE and ID8/IOSE), as well as enhancers preferentially active in normal human

epithelial cells (IOSE/OV8, IOSE/ID8, or both). The heatmap values denote the specificity, defined as the activity ratio between cell types.

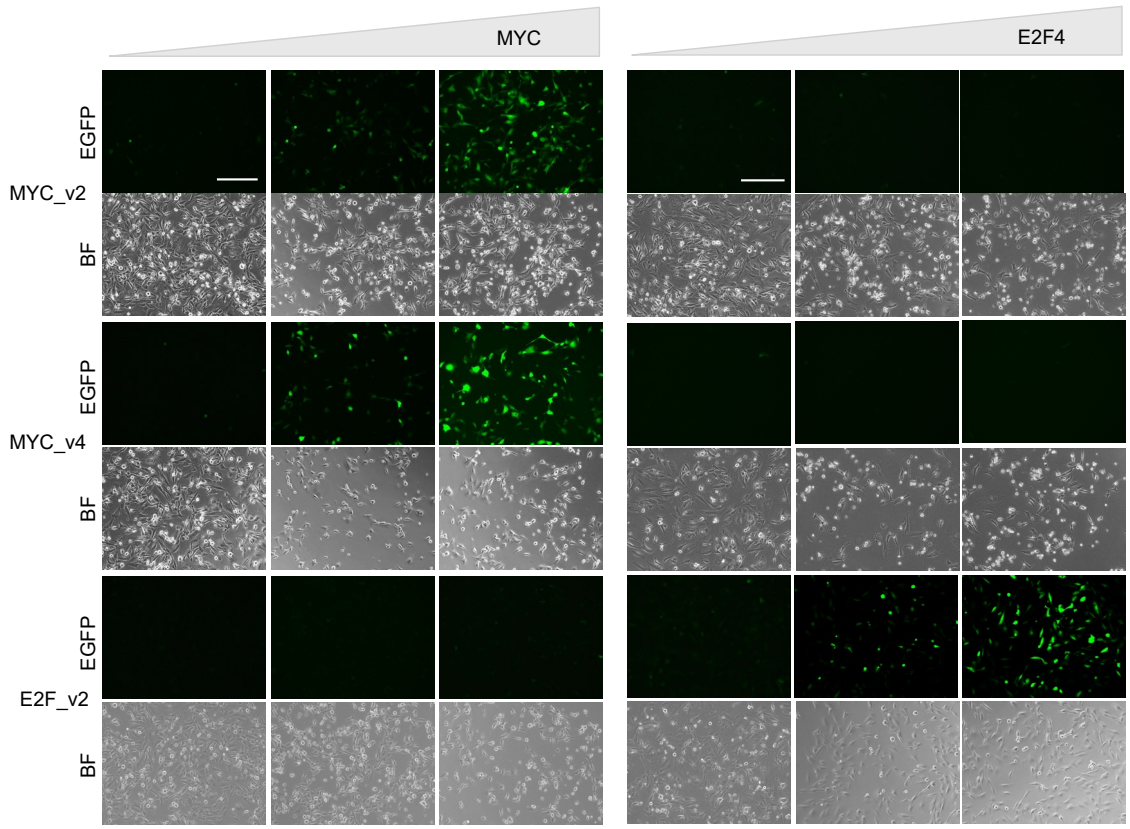

Extended Data Fig. 3. Dose-response of TREND-derived synthetic enhancers to TF abundance. Fluorescence microscopy images of IOSE cells co-transduced with MYC_v4 or E2F_v2 synthetic enhancers and a Tet-ON-inducible TF expression cassette for overexpressing MYC or E2F4. Images show graded reporter activation in response to TF abundance. Scale bar, 300 µm. Data are representative of three independent experiments.

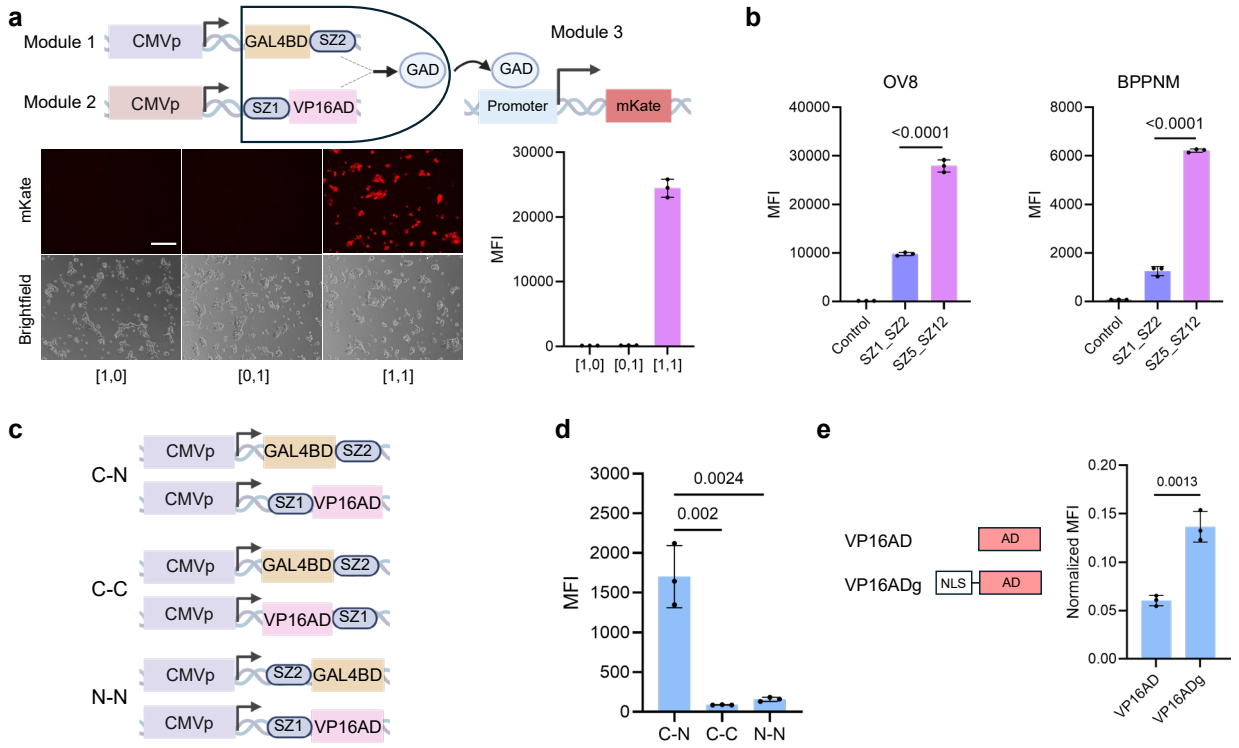

Extended Data Fig. 4. Orientation-dependent effects and nuclear localization enhance SYNZIP-based AND-gate performance. a, Reporter assays of partial AND-gate configurations, showing that incomplete circuits containing only one enhancer input ([1,0] or [0,1]) fail to activate transcription. Scale bar, 200 µm. **b,** Validation of SYNZIP-based AND-gate activity in human (OV8) and mouse (BPPNM) ovarian cancer cells. **c,** Schematic illustrating different orientations of SYNZIP fusion to GAL4BD and VP16AD domains. **d,** Quantification of reporter activity across different SYNZIP fusion orientations. **e,** Effect of a nuclear localization signal (NLS) to VP16AD on downstream reporter expression. Data represent mean ± s.e.m. from three independent experiments. Statistical significance was determined by unpaired two-tailed t-tests.

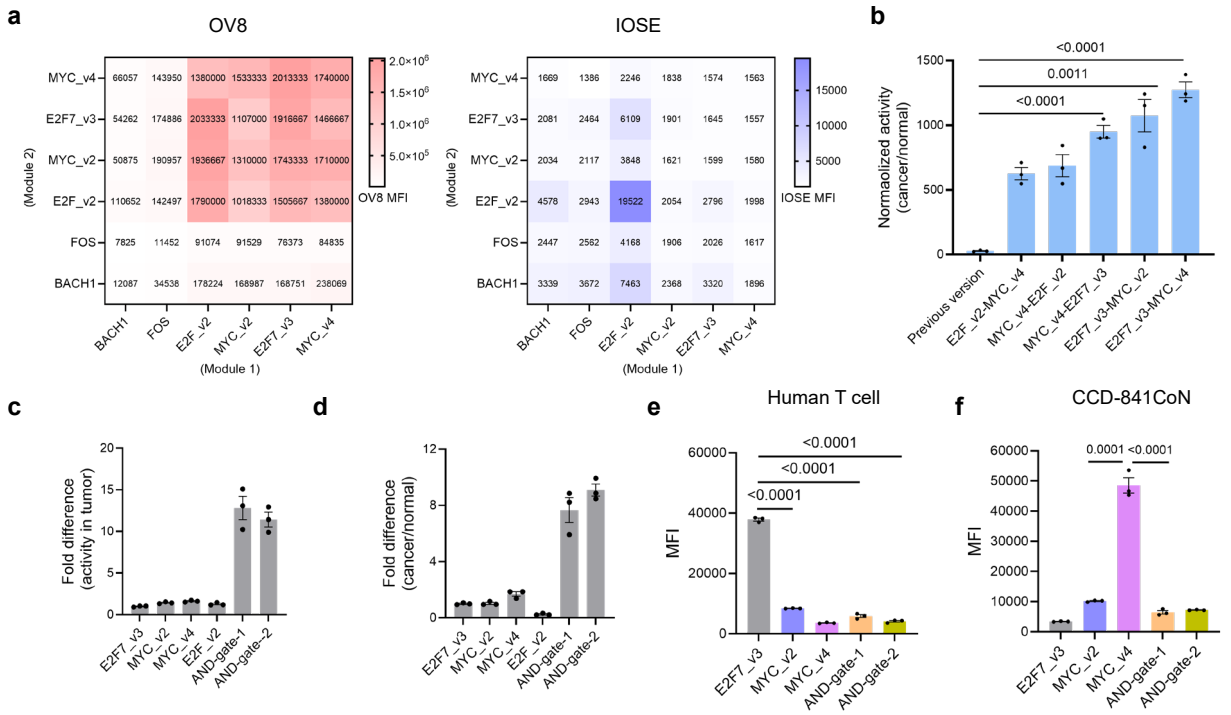

Extended Data Fig. 5. Functional evaluation of AND-gate circuits constructed from TREND-derived synthetic enhancers. a, Reporter assays comparing the activity of AND-gate constructs in OV8 and IOSE cells. Each construct was assembled from validated TREND-derived enhancers (MYC_v4, E2F7_v3, MYC_v2, E2F_v2, FOS, and BACH1), evaluated in different pairwise combinations. Heatmap values represent the mean from three independent experiments**. b,** Comparison of cancer specificity between the top five AND-gate designs and a previously published AND-gate configuration. Fold change represents the ratio of MFI in OV8 relative to IOSE. **c,** Quantification of transcriptional output from AND-gate constructs relative to single synthetic enhancers. AND-gate architecture amplifies output strength, with activity normalized to the E2F7_v3 single-enhancer group. **d,** Comparison of cancer-to-normal discrimination ratios between AND-gate and single-enhancer constructs. **e,f,** Reporter activity of single synthetic enhancers and AND-gate constructs in human T cells and normal colon epithelial CCD-841CoN cells. AND-gate-1 contains E2F7_v3 and MYC_v2 synthetic enhancers, and AND-gate-2 contains E2F7_v3 and MYC_v4 synthetic enhancers (**c-f**). Data are mean ± s.e.m. from three independent experiments. Statistical significance was determined by unpaired two-tailed t-tests.

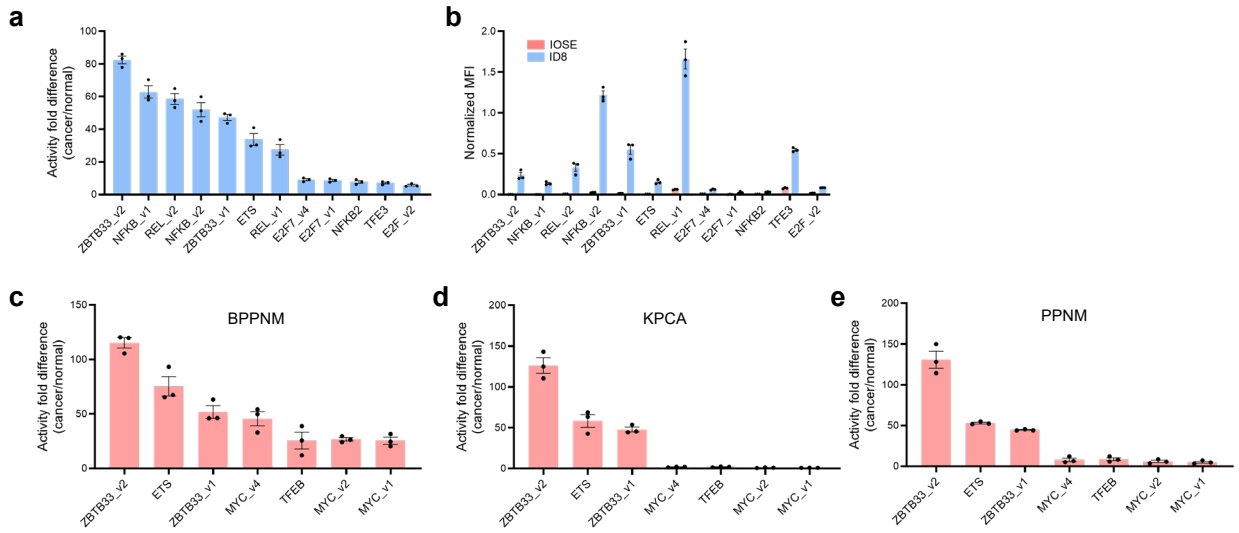

Extended Data Fig. 6. Screening and validation of murine cancer-specific synthetic enhancers. a, Tumor specificity of TREND-derived synthetic enhancers in ID8 mouse ovarian cancer cells, quantified as the fold difference in activity relative to normal human ovarian epithelial cells (ID8/IOSE). **b,** Normalized enhancer activity in ID8 and IOSE cells corresponding to the data in panel a, illustrating relative enhancer activity across cancer and normal contexts. MFI values were normalized to the UbC promoter control. **c-e,** Validation of synthetic enhancer activity across additional mouse ovarian cancer cell lines, including BPPNM **(c)**, KPCA **(d)**, and PPNM **(e)**. Activity fold difference represents the ratio of MFI in BPPNM/IOSE, KPCA/IOSE, and PPNM/IOSE, respectively. Data are mean ± s.e.m. from three independent experiments.

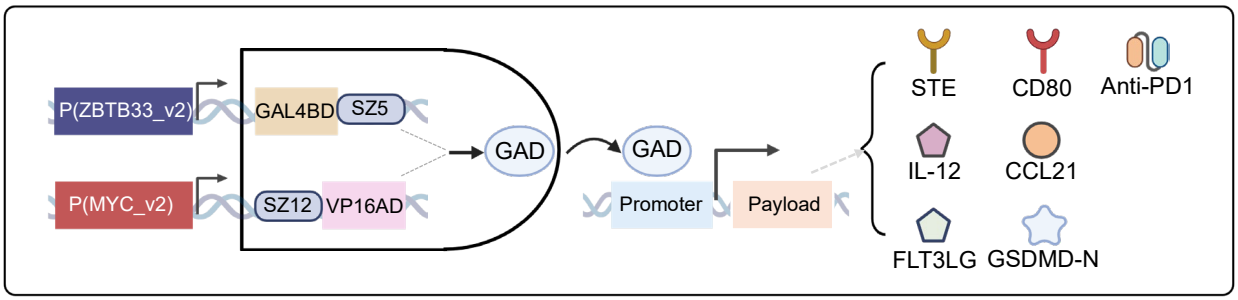

Extended Data Fig. 7. Schematic of the cancer-restricted AND-gate design. Two TREND-derived synthetic enhancers independently drive GAL4BD and VP16AD expression; coiled-coil pairing reconstitutes a synthetic transcription factor (GAD) that activates downstream therapeutic payloads, enabling cancer-selective expression of multiple immune effectors.

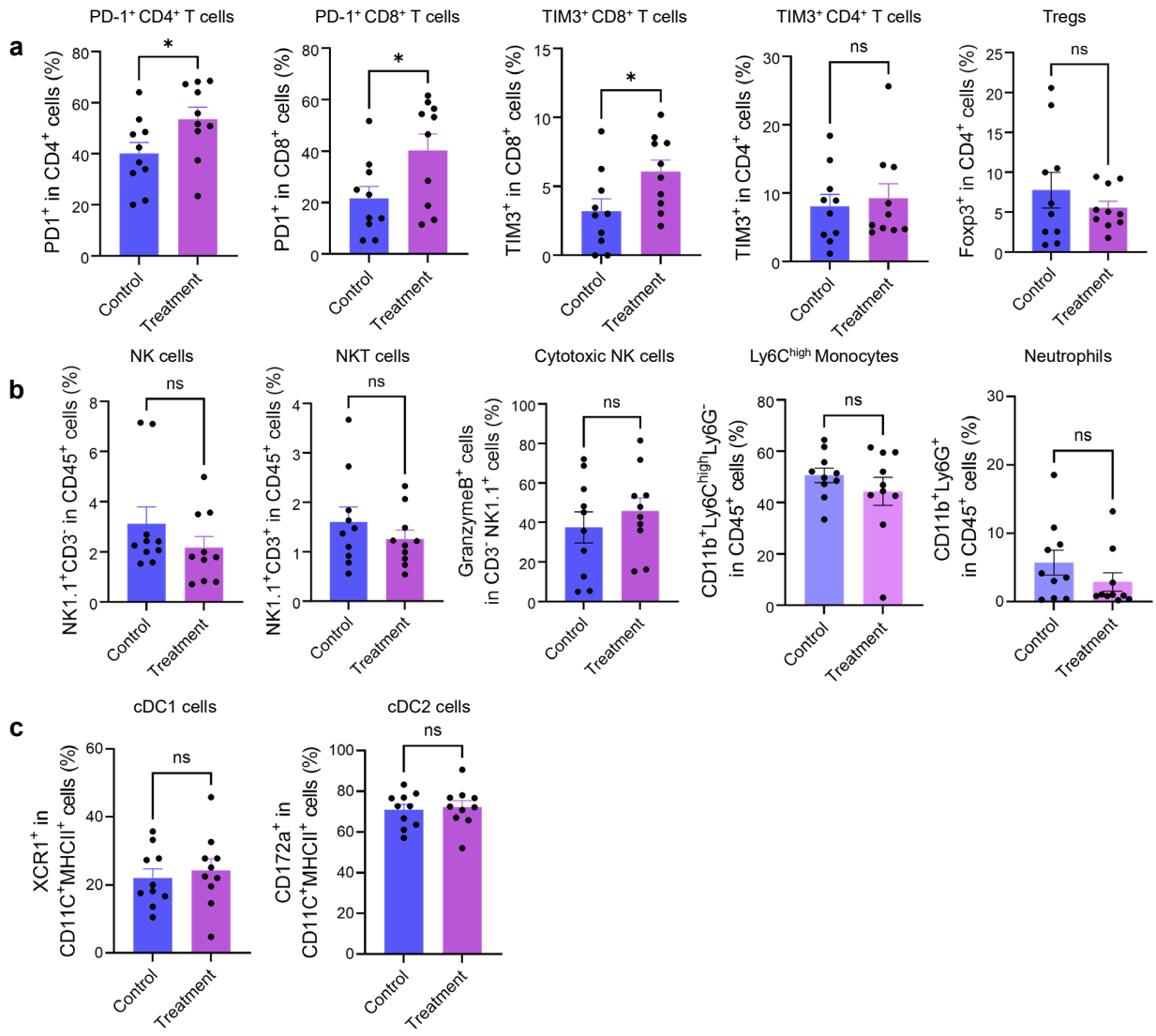

Extended Data Fig. 8. Characterization of tumor microenvironment (TME) immune composition following treatment with the AND-gate circuit expressing the S8IP output combination. a, Flow-cytometric analysis of T-cell subsets in the peritoneal TME, showing proportion of PD-1^{+} CD4^{+} T cells, PD-1^{+} CD8^{+} T cells, TIM-3^{+} CD8^{+} T cells, TIM-3^{+} CD4^{+} T cells, and Tregs. **b,** Proportion of innate immune populations including NK cells, NKT cells, cytotoxic NK cells, Ly6C^{high} monocytes and neutrophils. **c,** Proportion of cDC1 and cDC2 in the TME. Data represent mean ± s.e.m. from 10 mice per group. Statistical significance was determined by unpaired two-tailed t-tests.

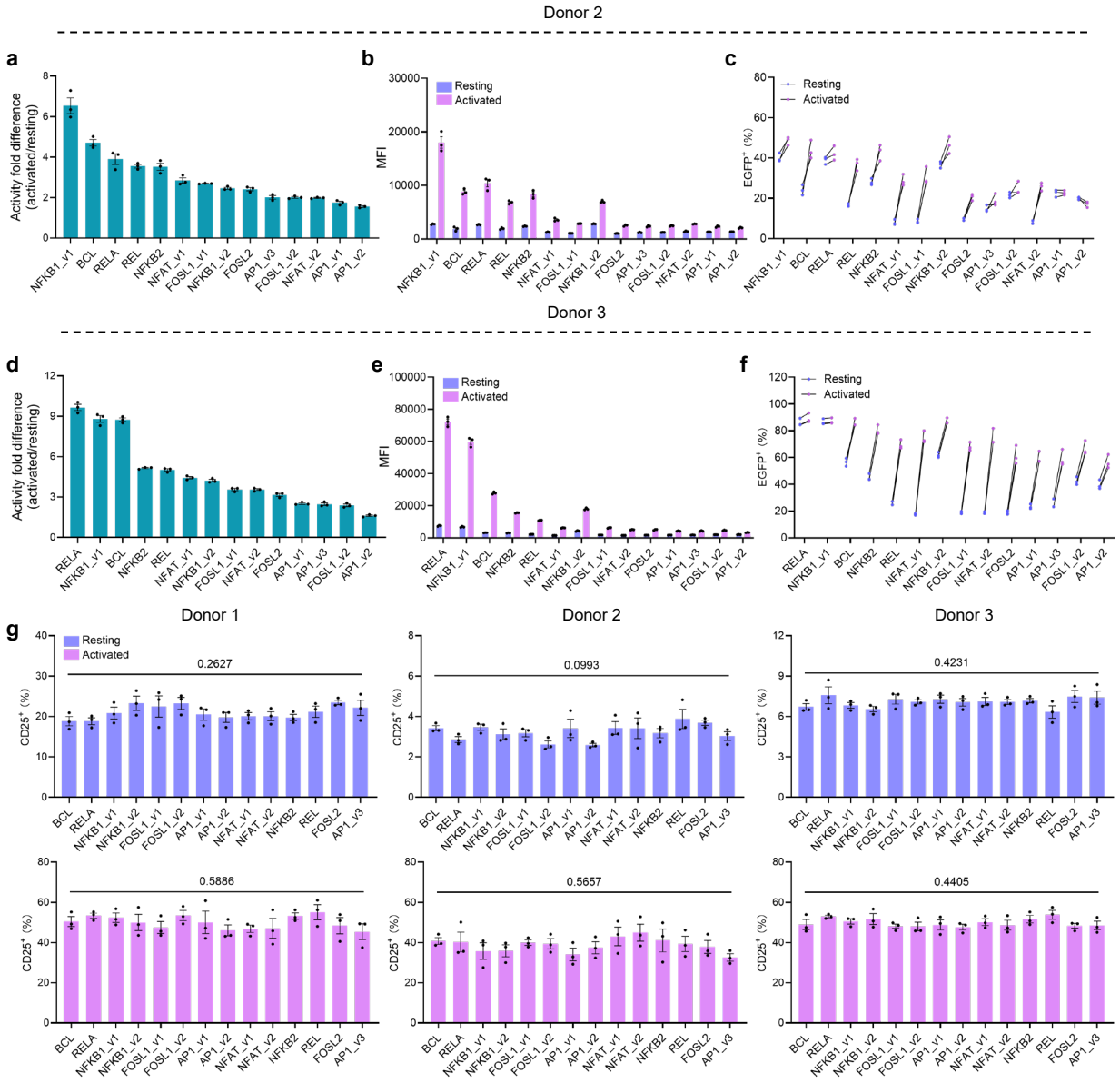

Extended Data Fig. 9. Validation of activation-responsive synthetic enhancers in primary human T cells. a,d, Fold change in reporter activity (activated/resting) for all tested enhancers, identifying candidates responsive to T-cell activation. **b,e,** Raw MFI of EGFP expression driven by individual enhancers under activated and resting conditions. **c,f,** Percentage of EGFP$^+$ T cells under activated versus resting conditions. **g**, Proportion of CD25$^+$ T cells transduced with individual enhancers under resting and activated conditions, summarized across three independent donors. Data represent mean ± s.e.m. from three independent experiments. Statistical significance was determined by unpaired two-tailed t-tests or one-way ANOVA.

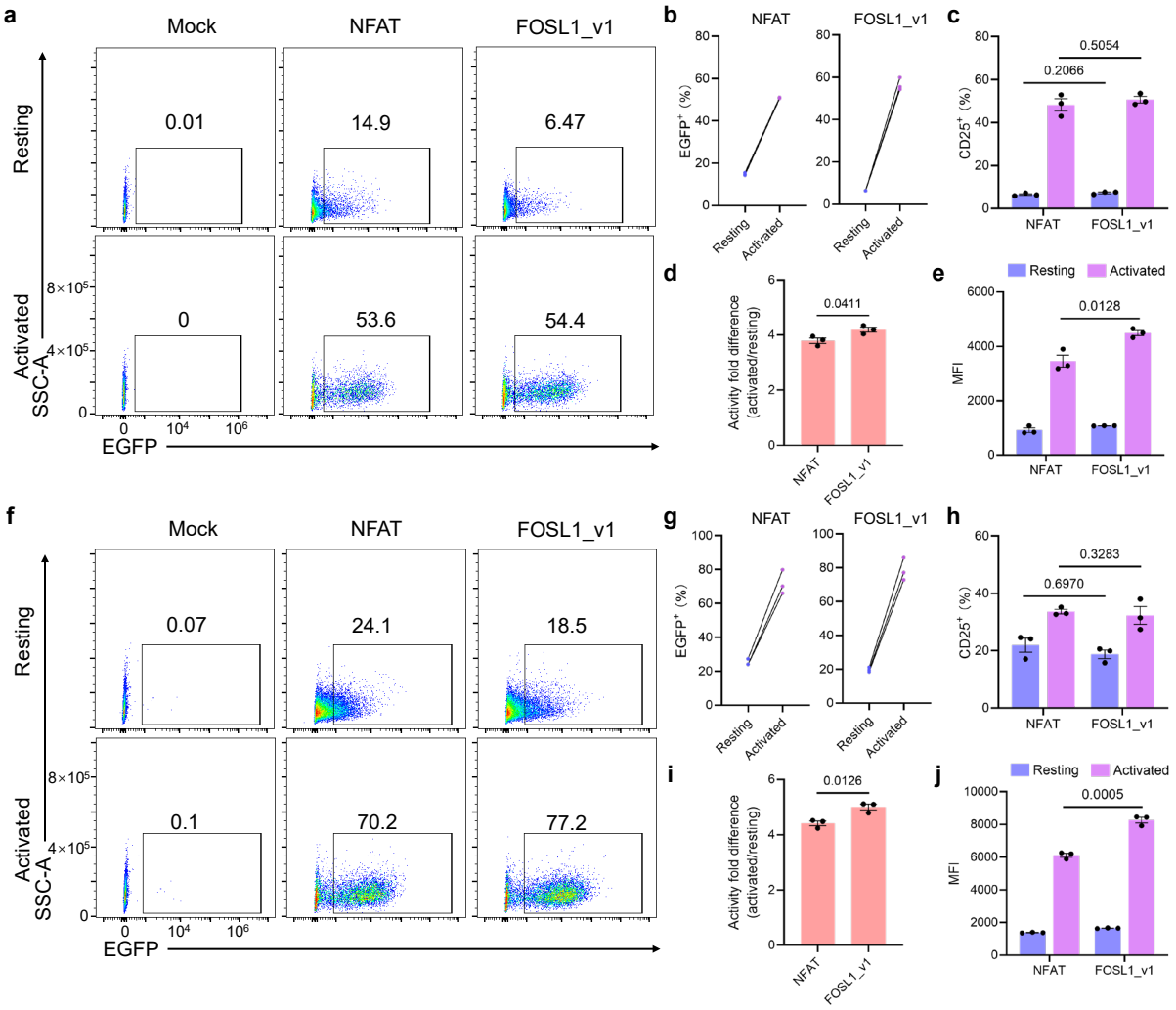

Extended Data Fig. 10. Comparison of NFAT and FOSL1-motif-based synthetic enhancer in T cells. a,f, Representative flow cytometry plots showing EGFP expression driven by NFAT and FOSL1_v1 enhancers in resting and activated T cells. **b,g,** Quantification of EGFP$^+$ cell percentages from panels (**a**) and (**f**). **c,h,** Proportion of CD25$^+$ T cells transduced with NFAT or FOSL1_v1 enhancers under resting and activated conditions. **d,i,** Fold change in reporter activity (activated relative to resting) for NFAT and FOSL1_v1 enhancers. **e,j,** MFI of EGFP expression for NFAT and FOSL1_v1 enhancers in activated and resting T cells. Panels **a-e** and **f-j** show data from two different donors. Data are mean ± s.e.m. from three independent experiments. Statistical significance was determined by unpaired two-tailed t-tests.